Thesis

Quantum Hall Effect in GaAs/AlGaAs Semiconductor Superlattice

Minoru Kawamura

Institute for Solid State Physics
University of Tokyo

December 2000

Preface

A two-dimensional electron gas (2DEG) exhibits the quantum Hall effect (QHE) when it is placed under a strong perpendicular magnetic field. As two-dimensionality is a prerequisite for the occurrence of the QHE, it is interesting to ask what happens when a degree of freedom for the motion perpendicular to the two-dimensional plane is introduced. This issue has been addressed theoretically and experimentally since the early stage of QHE research. Experimentally, Störmer *et al.* first demonstrated that the quantized Hall resistance and the vanishing diagonal resistivity is observed in a semiconductor superlattice.

In a quantum Hall phase, electronic states at the Fermi energy are localized. The localization length diverges as the Fermi energy approaches the center of the Landau subband. The exponent of the diverging localization length depends on the dimension of the system. In the case of semiconductor superlattice, the electronic states at the center of Landau level have a certain degree of three-dimensionality because of the dispersion relation along the growth direction. Therefore, in the semiconductor superlattice, the critical behavior near the center of Landau level is expected to differ from that in a single layer 2DEG.

The QHE in semiconductor superlattice has recently attracted renewed interest triggered by the theoretical prediction of the chiral surface state. In an isolated 2DEG in the quantum Hall state, all the bulk states at the Fermi level are localized so that the Hall current is carried by the edge channels. These edge channels are free from backscattering because of their chirality. For the integer quantum Hall state, the edge states are described in terms of chiral Fermi liquid. When the interlayer transfer is introduced, the edge states in different layers are coupled to form a conducting surface state. The existence of the chiral surface state was first demonstrated experimentally by Druist *et al.*

The experimental attempt to explore some aspects of the QHE in GaAs/AlGaAs semiconductor superlattice is described in this thesis. The paper is organized as follows. After a brief introduction of QHE, theoretical backgrounds of

QHE in three-dimensional systems and related experiments are reviewed in chapter 1. In chapter 2, the experimental procedure for sample fabrication and low-temperature measurement is described. Our experimental attempt to investigate the critical behavior in semiconductor superlattice is described in chapter 3. The vertical transport of semiconductor superlattice in the quantum Hall regime is described in chapter 4. A distinct non-Ohmicity and a large transverse magnetoresistance of the chiral surface state are discussed there. Finally, concluding remarks are described in chapter 5.

Contents

Chapter 1

Introduction

In this chapter, we review the theoretical backgrounds and experiments related to our topics. We first introduce the integer quantum Hall effect (QHE) and its edge channel description. After that the experiments focused on the transition from quantum Hall state (QHS) to Hall insulator (HI) in single layer two-dimensional electron gas (2DEG) systems are introduced. Next we turn our attention to the QHE in three-dimensional systems. After a historical review of the study of the QHE in three-dimensional systems, a theoretical work for the Anderson transition in semiconductor superlattice in high magnetic field is introduced. Finally, theoretical and experimental works of the chiral surface state are reviewed.

1.1 Integer quantum Hall effect

The most striking feature of the quantum Hall effect [1] is the remarkably precise quantization of the Hall resistance and the vanishing of diagonal resistance. It was in 1980 that von Klitzing *et al.* [2] observed unanticipated plateaus in the Hall resistance of a 2DEG, quantized to values,

$$R_{xy} = \frac{1}{i}\frac{h}{e^2}, \quad i = 1, 2, 3 \cdots. \tag{1.1}$$

The Hall resistance becomes plateau around $\nu = i$, where $\nu = nh/eB$ is the Landau level filling factor, n is the electron sheet density of the 2DEG and B is the magnetic field normal to the 2DEG.

When a perpendicular magnetic field is applied to a 2DEG, cyclotron motion with cyclotron frequency $\omega_{\mathrm{c}} = eB/m^*$ is brought about, where m^* is the effective mass of the electron. In a strong magnetic field, the angular momentum of the cyclotron motion is quantized, leading to the formation of discrete Landau levels,

$$E_N = \hbar\omega_{\mathrm{c}} \left(N + \frac{1}{2} \right), \quad N = 0, 1, 2, \cdots. \tag{1.2}$$

Each Landau level is broadened due to disorder. The half width of the disorder-broadened Landau subband Γ can be estimated by using the self-consistent Born approximation as

$$\Gamma = \sqrt{\frac{2}{\pi} \frac{\hbar}{\tau_0} \hbar\omega_{\mathrm{c}}}, \tag{1.3}$$

where τ_0 is the elastic scattering time. As temperature $T \to 0$, most electronic states in each Landau level are localized due to disorder, there exist extended states only at the center of each Landau subband. The Hall current is carried by these extended states below the Fermi energy E_{F}. In a quantum Hall state, the Fermi energy resides in the localized states between Landau subbands, giving rise to quantized Hall conductance and vanishing diagonal conductivity over a finite range of magnetic field.

1.2 Edge channel description

In the conventional experiments, the actual samples are shaped into the Hall bars which have finite width as shown in Fig.1.1. In this case, we can take the edge channel picture that the edge channels are formed along the edge of the sample and the current is carried by these edge channels. It was Halperin who introduced the idea of the edge channels [3]. In the edge channel description, the QHE is understood by the imperfect cancellation of the current of the up-going edge channels and down-going edge channels in Fig.1.1. This edge channel concept was further developed by Büttiker [4]. The edge channel picture is introduced by following Büttiker's theory.

We consider an ideal 2DEG, which has finite width as depicted in Fig.1.1. The top and bottom edges of the sample are connected to the electrodes and the left and right edges are defined by the electro-static potential with infinite height. Landau subbands are formed in the presence of perpendicular magnetic field. Around the left and the right edges of the sample, each Landau subband is bended up due to the confinement potential as seen in Fig.1.1. Suppose that the Fermi level lies between two Landau subbands in the bulk. Electrons in the left edge states flow from bottom to top and those in the right edge states flow in the opposite direction. Provided that the chemical potential of the bottom electrode μ_1 is greater than that of

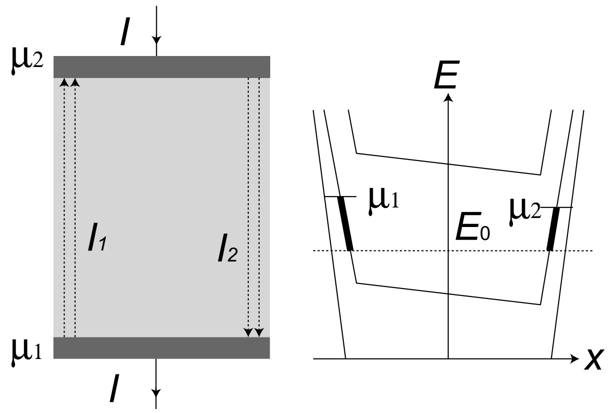

Figure 1.1: A schematic picture of sample with finite width (left) and its cross-sectional view of energy diagram (right).

top electrode μ_2, edge states below μ_1 are occupied in the left edge while they are occupied only up to μ_2 in the right edge because electrons in the left edge states come from the bottom electrode and electrons in the right edge states come from the top electrode. This non-equilibrium distribution between the left and the right edge states never relaxes in the sample because of the momentum conservation.

The presence of disorder does not fundamentally change this situation. Figure 1.2 shows a schematic drawing of equipotential line pattern in the presence of disorder. In the perpendicular magnetic field the electron wave function has an extent of the order of the magnetic length $l_B = \sqrt{\hbar/eB}$ around the equipotential line. Though disorder makes the equipotential line pattern irregular, the overlap of the wave function between the left edge states and the right edge states are exponentially small if the sample width is much larger than l_B. So, the scattering between the left edge channels and the right edge channels cannot occur. Thus electrons in an edge channel can continue to flow in one direction even in the presence of disorder.

To see how much current is carried by the edge channels, let us consider the one-body Hamiltonian with the Landau gauge $\vec{A} = (0, Bx, 0)$,

$$H = \frac{1}{2m^*}\left[p_x^2 + (p_y - eBx)^2\right] + U(x). \tag{1.4}$$

Here, the confinement potential $U(x)$ is assumed to be smooth in the y direction. The eigenstate of this Hamiltonian is written as

$$\psi(x, y) = \frac{1}{\sqrt{L_y}} \mathrm{e}^{-\mathrm{i}Xy/l_B^2} \phi(x), \tag{1.5}$$

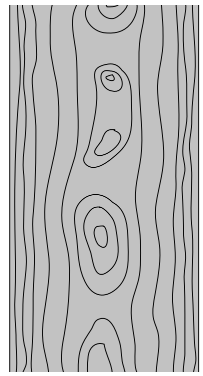

Figure 1.2: A schematic view of a equipotential line pattern in a 2DEG with disorder.

where $\phi(x)$ is the eigenfunction of the one-dimensional problem of $H_X\phi(x) = E(X)\phi(x)$. Here,

$$H_X = \frac{1}{2m^*}\left[p_x^2 + (eBX - eBx)^2\right] + U(x). \tag{1.6}$$

The expected value of the electron velocity along the edge for this eigenstate is described as

$$\begin{aligned}
v_y &= <\psi(x,y)|\frac{1}{m^*}(p_y - eBx)|\psi(x,y)> && (1.7)\\
&= <\phi(x)|\frac{1}{m^*}eB(X-x)|\phi(x)> && (1.8)\\
&= \frac{1}{eB}<\phi(x)|\frac{\partial H_X}{\partial X}|\phi(x)> && (1.9)\\
&= \frac{1}{eB}\frac{\partial}{\partial X}E(X). && (1.10)
\end{aligned}$$

The current carried by this eigenstate is $j = (e/L_y)v_y$. In order to obtain the total current carried by all electrons up to the chemical potential μ_1, we calculate the sum of j over all X which satisfies $E_0 < E(X) < \mu_1$. The current for each Landau level is described as

$$\begin{aligned}
I_1 &= \sum_X \frac{e}{L_y}v_y = \frac{L_y}{2\pi l_B^2}\int \mathrm{d}X\frac{e}{L_y}v_y = \frac{|e|}{h}\int \mathrm{d}X\frac{\mathrm{d}E}{\mathrm{d}X} && (1.11)\\
&= \frac{|e|}{h}(\mu_1 - E_0). && (1.12)
\end{aligned}$$

The net current is given by the difference between the current on one edge and that on the other flowing in the opposite direction.

$$I = I_1 - I_2 = \frac{|e|}{h}(\mu_1 - E_0) - \frac{|e|}{h}(\mu_2 - E_0) \quad (1.13)$$

$$= \frac{|e|}{h}(\mu_1 - \mu_2). \quad (1.14)$$

The voltage drop between the left and the right edge states $(\mu_1 - \mu_2)/e$ gives the Hall voltage. Therefore the resulting Hall conductivity $\sigma_{xy} = e^2/h$ is obtained.

From the above argument, we can construct a picture that in a quantum Hall state, current can flow along the edge in clockwise or counter clockwise direction depending on the magnetic field direction. This is the basic idea of the edge channel picture of QHE in a single layer 2DEG.

1.3 The QHS-HI transition

In this section, we introduce experimental studies in single layer 2DEGs which focused on the critical behavior at the mobility edges at the center of each Landau subband.

The electron localization effect in disordered system is known as Anderson localization. Localized states are characterized by the localization length $\xi(E)$. As the mobility edge E_c is approached, the localization length diverges as

$$\xi(E) \propto |E - E_c|^{-\mu}. \quad (1.15)$$

It is generally believed that the critical behavior near the mobility edges should show certain universal features, *i.e.* should only be determined by the fundamental symmetries of the system, such as dimensionality or time reversal symmetry, and not depend on the detailed microscopic nature of the disorder.

In a quantum Hall phase, electronic states at the Fermi energy are Anderson localized in the bulk of a sample as described in the section 1.1. Each Landau level is broadened due to the presence of disorder. The most part of the disorder-broadened Landau subband consists of localized states, and there exists the mobility edge E_c at the center of Landau subband. The critical exponent $\mu = 2.35 \pm 0.3$ is determined for 2D systems at the center of Landau subband by the numerical simulation and the finite size scaling method [7].

As the magnetic field is swept, the electronic state at the Fermi energy changes from localized to extended and then vice versa, corresponding to

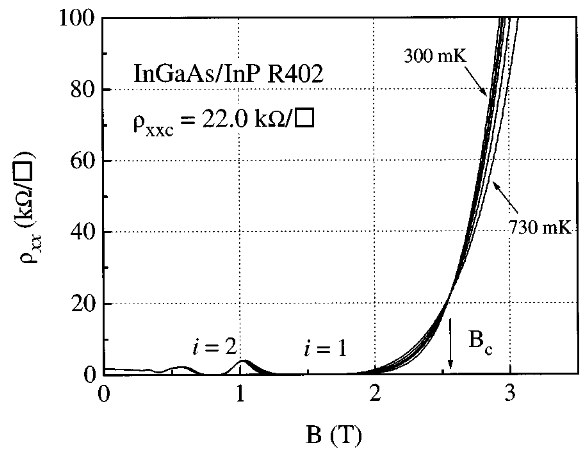

Figure 1.3: Experimental data by Pan *et al* [6]. The magnetic field dependence of ρ_{xx} at T = 300, 390 450, 510, 600 and 730 mK.

the QHE plateau-plateau transitions. The first quantitative study of the transition between two integer quantum Hall states was performed by Wei *et al* [5]. The experiment was done in an InGaAs/InP heterostructure. The maximum value of the first derivative of the Hall resistance ρ_{xy} with respect to B, *i.e.* $(\mathrm{d}\rho_{xy}/\mathrm{d}B)^{\max}$ scales as $T^{-\kappa}$ with $\kappa = 0.42$. These scaling results imply that the transport coefficients near the critical magnetic field B_c are functions of a single scaling parameter $|B - B_\mathrm{c}|/T^\kappa$. The critical exponent κ, which is related to the critical exponent of the localization length μ by $\kappa = 1/z\mu$, is in good agreement with the theoretically obtained $\mu = 2.3$ if one takes the dynamical exponent as $z = 1$.

The QHS-HI transition provides another stage to investigate the critical behavior in magnetotransport measurement. In Fig.1.3, the result of a representative experiment [6] is displayed. The sample was an InGaAs/InP heterostructure. The magnetic field dependence of the diagonal resistivity ρ_{xx} was measured at several temperatures. All the ρ_{xx} versus B curves at different temperatures cross at a critical magnetic field B_c, *i.e.* ρ_{xx} is independent of temperature at $B = B_\mathrm{c}$. On the lower field side of B_c, ρ_{xx} decreases as the temperature is lowered and ρ_{xx} increases with decreasing temperature on the higher field side.

As shown in Fig.1.4, all the temperature dependent data collapse onto a single curve by performing temperature-scaling analysis with scaling parameter $|B - B_\mathrm{c}|/T^\kappa$. The obtained value of $\kappa = 1/z\mu = 0.45$ shows that this transition belongs to the same universality class as the above mentioned

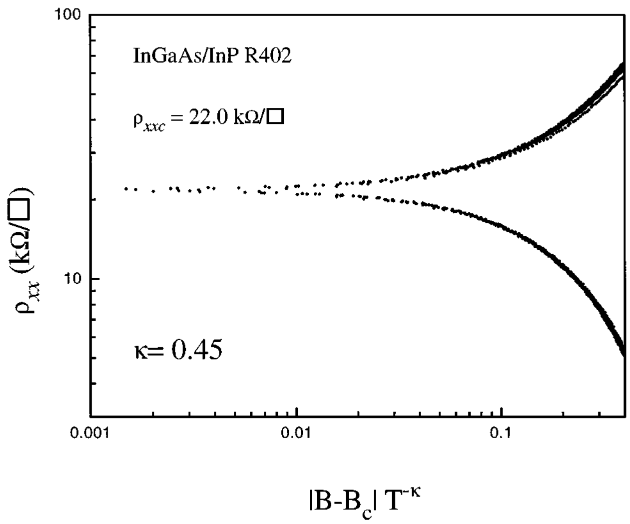

Figure 1.4: ρ_{xx} versus $|B - B_{\mathrm{c}}|/T^{\kappa}$ with parameter κ adjusted to be 0.45 to collapse the data points at different temperatures [6].

plateau-plateau transitions. For these QHS-HI transitions, the value of the diagonal resistivity ρ_{xx}^{c} at the critical point is very close to h/e^2 as theoretically predicted.

1.4 QHE in three-dimensional systems

In the following sections, we review the QHE in three-dimensional (3D) systems.

As two-dimensionality is an essential prerequisite for the occurrence of QHE, it is interesting to ask what happens when a degree of freedom for the motion perpendicular to the 2D plane is introduced. This issue has been addressed both theoretically and experimentally since the early 1980s [8, 9, 10, 11]. For example, Azbel has considered this problem for highly anisotropic materials [8]. He argues that the vanishing diagonal resistivity occurs in the limit of high magnetic field in the anisotropic 3D system.

Störmer *et al.* [11] first demonstrated that the quantized Hall resistance and the vanishing diagonal resistivity can be observed in GaAs/Al$_x$Ga$_{1-x}$As semiconductor superlattice. Their superlattice consists of 30 units of 18.8 nm wide well layer and 3.8 nm wide barrier layer. The Al content of $x = 0.18$ was chosen for the barrier layer. Only the central 2.5 nm of the barrier layer was doped with Si to 1×10^{18} cm^{-3}. The electron density $n = 2.1 \times 10^{17}$

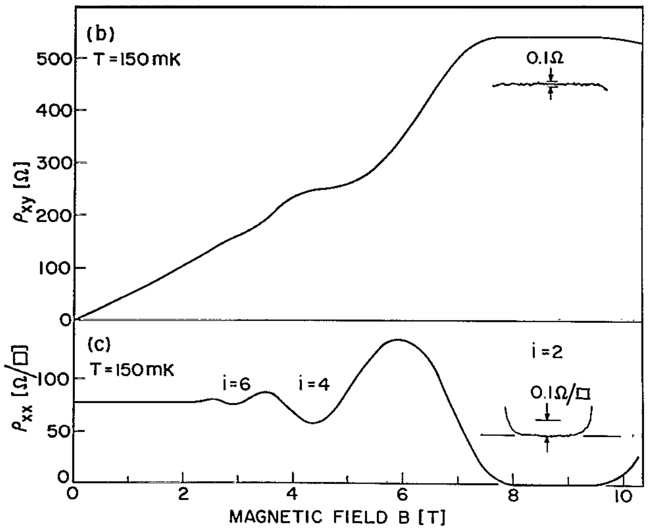

Figure 1.5: Experimental data by Störmer *et al* [11]. The magnetic field dependence of (b) Hall resistance ρ_{xy} and (c) diagonal resistivity ρ_{xx} at $T =$ 150 mK in the GaAs/AlGaAs semiconductor superlattice.

cm^{-3} and the Hall mobility $\mu_{\mathrm{H}} = 6400$ cm^2/Vsec was obtained from the magnetotransport measurement at 4.2 K. Only the first miniband of the superlattice is occupied. Figure 1.5 shows the magnetic field dependence of Hall resistance ρ_{xy} and the diagonal sheet resistivity ρ_{xx}. The quantized ρ_{xy} and the vanishing diagonal resistance ρ_{xx} is observed.

In a 3D system, each Landau level develops into a band. Since the dispersion relation along the growth direction (z-direction) is not affected by the magnetic field parallel to z, the shape of each band is field-independent and reflects the one-dimensional density of states of the k_z-dispersion with its width $4t$. In high magnetic field where $\hbar\omega_{\mathrm{c}}$ exceeds $4t$, the density of states exhibits gaps as in the ideal 2D case, and the condition for the observation of the QHE is fulfilled.

The QHE in other 3D systems have been studied in such layered materials as organic conductors and Mo oxides. Quantization of the Hall resistance has been reported in $(TMTSF)_2PF_6$ [13, 14] and η-Mo_4O_{11} [12]. In these materials, the QHE is brought about by Landau quantization of tiny residual pieces of Fermi surface left over from the imperfectly nested original quasi-one-dimensional Fermi surface.

1.5 Anderson transition in three-dimensional systems in magnetic field

A critical behavior near the mobility edge at the center of Landau subband is examined numerically in the multilayered 2DEGs with weak interlayer coupling in the presence of strong magnetic field by Ohtsuki *et al* [10]. Their work is introduced in this section.

A stack of 2D disordered electron systems with a magnetic field perpendicular to the layers is considered. Allowing interlayer hopping of electrons, one obtains an effectively 3D system. The electron motion perpendicular to the 2D plane is treated in tight binding model with band width $4t$. The limit of strong magnetic field where the inter-Landau subband mixing can be neglected is considered. The corresponding Hamiltonian is written as

$$H = -t\sum_{X,i}(|X,i><X,i+1| + \mathrm{c.c}) + \sum_{X,X',i}|X,i> V^i_{X,X'} < X',i|, \tag{1.16}$$

where i is the layer index, X denotes the center coordinate, t is the interlayer transfer integral and $V^i_{X,X'}$ is the matrix elements of the random potential between the Landau states within the i-th layer. The random potential is assumed to be statistically uncorrelated at different sites. The localization length of the finite size system is numerically calculated from the one-body Green function. The finite size scaling method was employed to determine the critical exponent.

In the clean limit, the density of states consists of a series of Landau subbands with the band width $4t$. These subbands are further broadened by disorder to the width $4t + 2\Gamma$. Each Landau subband consists of a central band of three-dimensionally extended states with localized tails on each side.

The critical exponents μ determined for different values of $2t/\Gamma$ are listed in the table 1.1. All the values of μ are independent of $2t/\Gamma$, within the error bars. They coincide with the result obtained in the limit of zero magnetic field for 3D Anderson model, $\mu = 1.5$. Compared with the single layer 2DEG in the quantum Hall phase, where $\mu \sim 2.3$, the critical exponent is reduced by a factor of 3/5 in the weakly coupled multilayered quantum Hall systems. As μ is independent of interlayer coupling parameter $2t/\Gamma$ in the region where the data and their evaluation is reliable ($2t/\Gamma > 0.15$), they concluded that the crossover between μ(2D) and μ(3D) must occur at infinitesimally small $2t/\Gamma$.

Similar result for the critical exponent of the Anderson transition in 3D systems in strong magnetic field is obtained from another model (network model) [15].

$2t/\Gamma$	μ
0.9	1.45
0.6	1.38
0.3	1.35
0.15	1.24
0.075	0.94

Table 1.1: The critical exponent μ as function of the interlayer coupling parameter $2t/\Gamma$ [10].

1.6 Chiral surface state

The existence of the metallic state at the periphery of the multilayered quantum Hall system was first pointed out by Chalker and Dohmen [15]. In an isolated 2DEG in the quantum Hall state, all bulk states at the Fermi level are localized so that the current is carried by the edge channels as described in section 1.2. These edge channels are free from backscattering because of their chirality. When the 2DEGs in the quantum Hall state are stacked and the interlayer charge transfer is allowed between them, the edge channels in different layers are coupled to form a conducting surface state. This conducting state formed at the surface of the multi-layered quantum Hall system is referred to as a "chiral surface state". Much theoretical effort was done to reveal the properties of the chiral surface state.

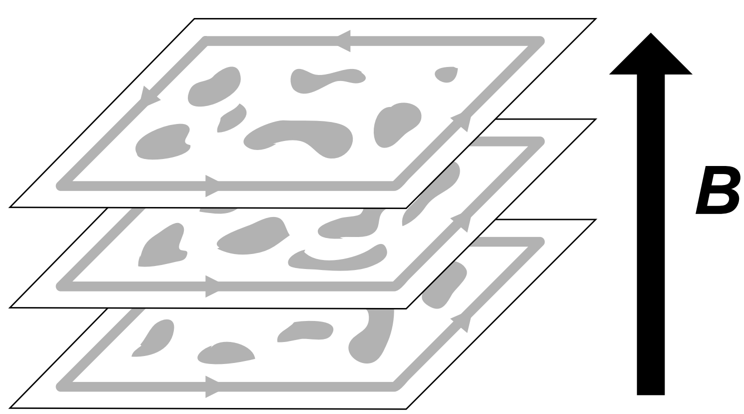

Figure 1.6: A schematic view of multi-layered quantum Hall system. All the bulk states are localized, while extended edge channels surround the sample.

One of the striking features of the chiral surface state is its metallic nature with small sheet conductivity. In usual 2D electron system in the absence of magnetic field, all the electronic states are localized due to quantum interference effects. In the presence of perpendicular magnetic field, metallic states with conductivity of e^2/h are created at the center of each Landau subband. However, away from the center of the Landau subband, all the electronic states are localized and the conductivity vanishes rapidly as temperature $T \rightarrow 0$. According to Balents and Fisher [16], any interference effects are suppressed in chiral surface states despite their 2D character because of the chiral nature of the electronic motion along the edge channel. In the quantum Hall states, as all the bulk states are localized at temperatures well below the bulk QHE gap $\hbar\omega_c/2$, the surface states dominate the z-axis transport at these low temperatures. In this regime, we expect to have N surface sheaths (N being the number of filled Landau levels) which give a temperature independent sheet conductivity

$$\sigma_{zz} = N\frac{e^2t^2\tau a}{2\pi\hbar^3 v} = N\frac{e^2t^2 l_{\mathrm{el}} a}{2\pi\hbar^3 v^2}. \tag{1.17}$$

Here, a is the interlayer spacing, t is the interlayer transfer integral, τ is the elastic scattering time, v is the electron velocity in the chiral direction and $l_{\mathrm{el}} = v\tau$ is the elastic scattering length. Thus, despite their 2D character, the chiral surface states are expected to remain metallic at low temperatures, even if their conductivity is considerably smaller than e^2/h.

The magnetoresistance of the chiral surface state is discussed by Chalker and Sondhi [17]. They have shown that the magnetoresistance is described in a simple Drude-like formula,

$$\sigma_{zz}(B_\parallel) = \frac{\sigma_{zz}(B_\parallel = 0)}{1 + (B_\parallel/B_0)^2}, \tag{1.18}$$

with $B_0 = \Phi_0/a l_{\mathrm{el}}$. Here, $\Phi_0 = h/e$ is the flux quantum. This simplicity is also the consequence of the elimination of multiple scattering processes due to the chiral motion along the edge. The conductivity in the absence of parallel magnetic field $\sigma(B_\parallel = 0)$ depends on two unknown quantities, the elastic scattering length l_{el} and the electron velocity v in the chiral direction, while B_0 involves only the first one. Thus the study of magnetoresistance of the chiral surface state provides a way to determine these quantities separately.

Furthermore, the metal-insulator transition driven by the geometrical parameters of the samples and conductance fluctuation in the chiral surface state is discussed by several authors [18, 19, 20]. Effects of interactions and disorder in the chiral surface states are also discussed in a recent paper [21].

The first experimental study focused on the chiral surface state in GaAs/AlGaAs semiconductor superlattice was performed by Druist *et al* [22]. The magnetic

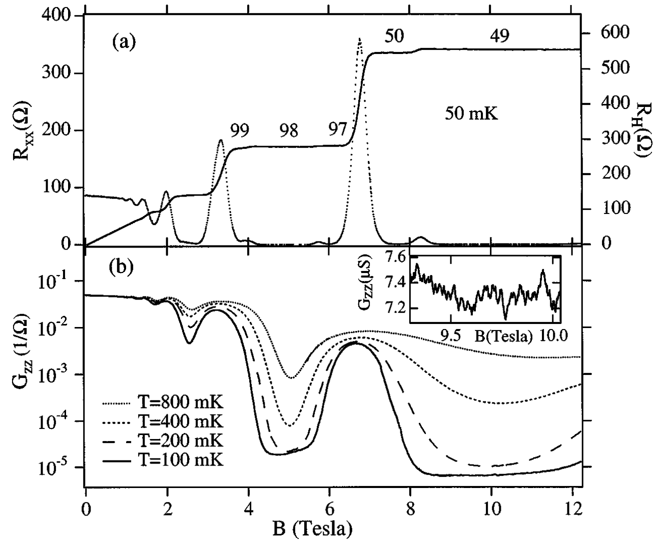

Figure 1.7: (a) In-plane transport at 50 mK. The QHE at $\nu = 1, 2, 4$ are clearly seen. (b) Vertical conductance G_{zz} of the 150 μm square mesa at different temperatures versus magnetic field. In quantum Hall states, G_{zz} saturate to a finite low-temperature value when the surface states dominate the vertical transport [22].

field dependence of the vertical conductance G_{zz} develops deep minima when the in-plane transport shows QHE as displayed in Fig.1.7. Figure 1.8 shows the temperature dependence of G_{zz} in the quantum Hall states. As the temperature is decreased, G_{zz} in the quantum Hall states initially drops rapidly. However, as the temperature falls below 200 mK, the conductance at the center of quantum Hall states appears to reach a constant value. The low temperature saturating values of G_{zz} for the mesas with different sizes are not proportional to mesa cross-section, but proportional to mesa perimeter. The fact that the low temperature conductance is proportional to mesa perimeter indicates that the current flows on the surface of the mesas. Almost temperature independent sheet conductivity of $\sigma_{zz} = 1.2 \times 10^{-3} e^2/h$ is obtained, which is much smaller than e^2/h. The observed vertical sheet conductivity, which is much smaller than e^2/h is almost independent of temperature at low temperatures. The existence of surface states at the periphery of the multilayered quantum Hall system is thus confirmed experimentally.

Formation of chiral surface state is also discussed in the study of organic conductors and Mo-oxides [12, 23, 24]. It is reported that the temperature dependence of the Shubnikov-de Hass oscillation amplitude in α-(BEDT-

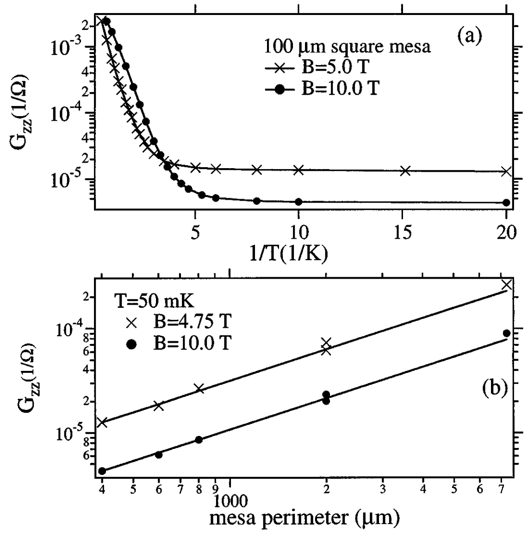

Figure 1.8: (a) The temperature dependence of G_{zz}. (b) The mesa size dependence of G_{zz} at low temperature. Good fits to lines with slope = 1 show that G_{zz} is proportional to C, indicating that the current flows on the surface of the mesas [22].

TTF$)_2$KHg(SCN$)_4$ deviates from the conventional Lifshitz-Koshvich theory. The deviation is explained in terms of the formation of chiral surface state. Although the saturation in the temperature dependence of G_{zz} in the quantum Hall regime is reported for these systems, the direct evidence that the conductance is dominated by surface states is not obtained, because it is difficult to define the sample sizes in these materials.

Chapter 2

Experimental

In this chapter, the experimental methods including the design of superlattice, the sample fabrication techniques and low-temperature measurement methods are described.

2.1 Sample

2.1.1 Design of superlattice

A great progress of the semiconductor crystal growth technique using molecular beam epitaxy (MBE) method has allowed us to study low dimensional electronic systems. The semiconductor superlattice system offers a unique medium where the band structures can be controlled by adjusting the barrier width, barrier height and well width. One of the early demonstrations of artificial electronic band structure was made by Chang *et al.*, who observed the Shubnikov-de Hass oscillations in GaAs/AlGaAs superlattices and discussed in terms of mini gap and miniband formation associated with the superlattice periodicity [25].

In a semiconductor superlattice, periodicity along the growth direction (z-direction) leads to formation of one-dimensional subbands and subgaps in the energy dispersion along the k_z-direction. Figure 2.1 shows the miniband structure of superlattice A used in the present study, calculated by the simplest Kronig-Penny model. Non-parabolicity of the conduction band and the slight difference in effective mass between GaAs and AlGaAs are neglected. A band bending effect caused by the charge transfer from the barrier layer to the well layer is also neglected. The calculated first miniband width along the k_z-direction is $4t = 0.12$ meV.

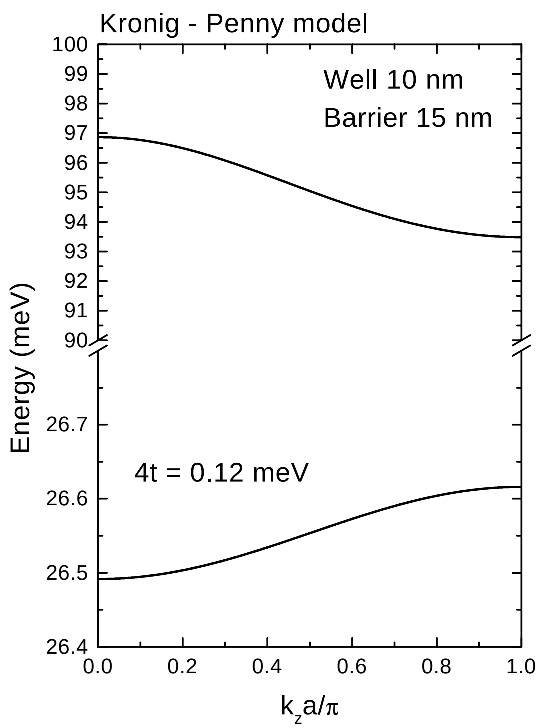

Figure 2.1: The dispersion relation along the k_z-direction calculated by the Kronig-Penny model for superlattice A used in the present study.

Superlattice	Barrier height (meV)	Barrier width (nm)	Well width (nm)	Subband width $4t$ (meV)
A	120	15	10	0.12
B	120	12	10	0.42
C	120	10	10	0.95
D	120	8	10	2.1
E	120	6	10	4.8

Table 2.1: Parameters of the superlattice used in the present study. Sample A consisted of 100 units of GaAs and AlGaAs layer and the others consisted of 50 units of GaAs and AlGaAs layer.

2.1.2 MBE growth

The wafers used in this work were grown by MBE [26]. They were grown in pairs of identical superlattices. One wafer for the vertical transport measurement was grown on an n^+GaAs(100) substrate and capped with a heavily doped layer. A second one for lateral transport measurement was grown on a semi-insulating GaAs(100) substrate. The parameters of the superlattice used in the present study is summarized in table 2.1. In the case of superlattice A, the superlattice part consisted of 100 units of GaAs well layer and $Al_xGa_{1-x}As$ barrier layer. Only the central part (5 nm) of each $Al_xGa_{1-x}As$ layer was doped with Si donors as shown in Fig.2.2. The Si doping density of $N_D = 8.0 \times 10^{23}$ m^{-3} was chosen so as to make the Fermi energy lie in the first minigap to form a weakly corrugated cylindrical Fermi surface. The relatively low Al content of $x = 0.15$ was chosen for the barrier layer to achieve a sufficiently large interlayer transfer integral t along the growth direction. The growth of the superlattice part was performed at a relatively low substrate temperature, about 540 °C, in order to prevent diffusion of the Si donors. Reflection high-energy electron diffraction (RHEED) method was employed to monitor the growth. The intensity of the RHEED oscillates corresponding to the layer-by-layer growth. The growth rates of GaAs and AlGaAs are obtained from the period of the RHEED oscillation. The well width, the barrier width and the Al content in table 2.1 were determined through the period of the RHEED oscillation.

2.1.3 Sample fabrication

For the lateral transport measurement, standard Hall bar-shaped samples were fabricated by photolithography and wet chemical etching. The size of the Hall bar is 50 μm $\times$ 200 μm. The van der Pauw-type samples were also

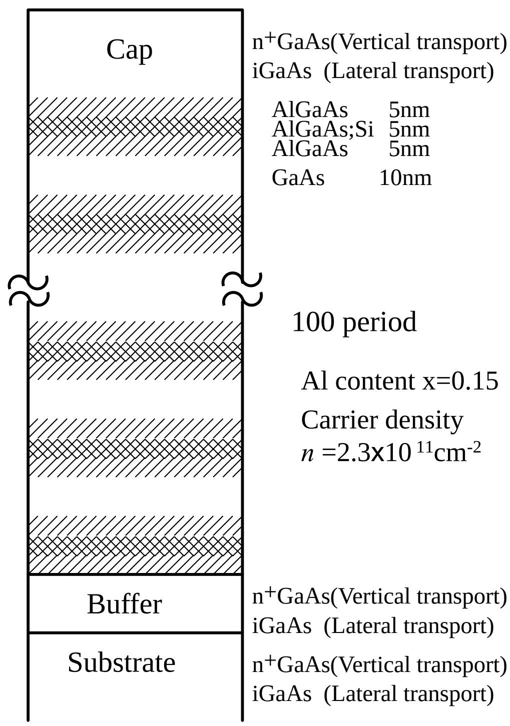

Figure 2.2: A schematic picture of the growth profile of superlattice A

used for the lateral transport. They were achieved by putting indium dot contacts on the corners of the square samples. The size of those samples were about 3 mm × 3 mm.

For the vertical transport measurements, square columnar mesas were fabricated by photolithography and wet chemical etching. A schematic picture of the sample for the vertical transport measurement is shown in Fig.2.3. The fabrication procedure was as follows.

1. AuGe alloy was deposited on the back of the substrate.

2. AuGe was patterned by usual photolithography technique on the front of the substrate. The thickness of AuGe film was typically 700 Å.

3. In order to obtain Ohmic contact, the sample chip was annealed at about 400 °C for 5 minutes in the atmosphere of pure N_2. Alloying was done at relatively low temperature in precaution that Ge do not diffuse into the superlattice part.

4. Hard baked photoresist was patterned by standard photolithography in order to protect the AuGe contact during the etching process.

5. The square columnar mesa was etched for about 5 minutes in H_2O_2: H_3PO_4: H_2O = 1: 1: 8 solution at room temperature.

6. Au was deposited to spread the top electrode after coated with the photoresist OMR83 (a few μm thick) as an insulating layer.

Four mesas with different cross-sections of $50{\times}50$ μm^2, $100{\times}100$ μm^2, $200{\times}200$ μm^2 and $400{\times}400$ μm^2, were simultaneously fabricated on a single chip. The two terminal current-voltage (I-V) characteristics at 4.2 K in zero magnetic field assured that the perfect Ohmic contact was achieved.

2.2 Magnetotransport measurement

Magnetotransport measurements were carried out in superconducting solenoids typically up to 15 T. Two types of ^{3}He-^{4}He dilution refrigerators were used for the low temperature measurement ranging from 500 mK to 20 mK. One of the dilution refrigerators used in the present study was top-loading type, which was equipped with a rotating sample holder. This enabled us to rotate samples in the mixing chamber at low temperature. Temperature was monitored by ruthenium oxide resistance thermometers which were set near the sample. Standard ac lock-in techniques were employed for the resistance

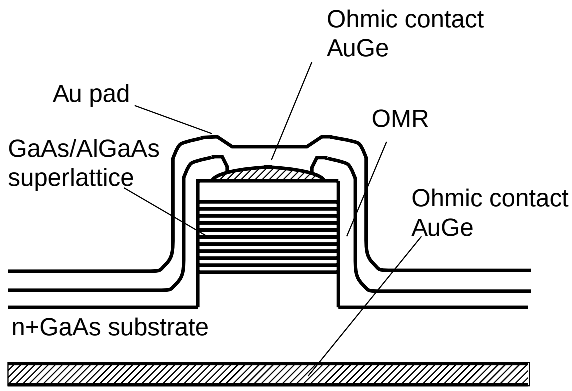

Figure 2.3: Schematic picture of a sample for the vertical transport measurement.

measurement. The measurement frequencies were typically set at about 20 Hz.

Since the resistance thermometers generally have magnetoresistance, it is not easy to determine temperature in the presence of magnetic field. Particularly, no alternatives are conventionally available at the temperature range of dilution refrigerator. The calibration of the ruthenium oxide resistance thermometer (which was well calibrated in the absence of magnetic field) was extended to the high magnetic field region in the following way. In Fig.2.4, a schematic view of the measurement system with a top-loading type dilution refrigerator is depicted. As the top part of the mixing chamber is located outside the superconducting solenoid, magnetic field is small there. Furthermore, this part of the mixing chamber of this system [27] is surrounded by a superconducting coil so that the effect of the magnetic field is much reduced. Two ruthenium oxide resistance thermometers were used. One (RuO1) was placed in the top part of the mixing chamber and the other (RuO2) was set near the sample. The magnetic field dependence of RuO2 was monitored while the temperature was controlled. The thermometer RuO1 was used to regulate the temperature of the mixing chamber. By keeping the field sweep slow enough so that the dilute phase of ^{3}He-^{4}He mixture was always in equilibrium during the field sweep, the magnetoresistance curve of RuO2 was obtained at several temperatures. Thus the calibration curve of the thermometer RuO2 is extended to the presence of magnetic field.

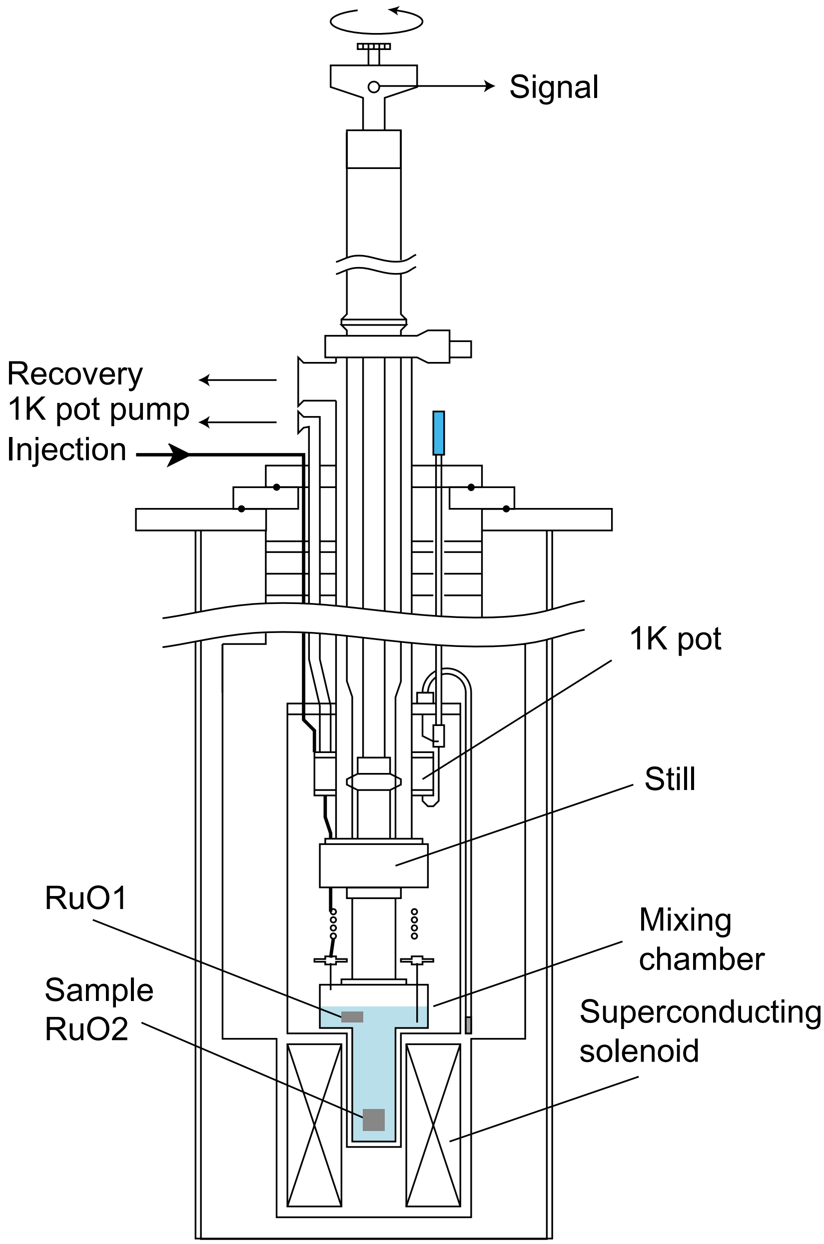

Figure 2.4: A schematic view of the top-loading type dilution refrigerator. The sample holder equipped with gear assembly enables us to rotate samples at low temperature. Two ruthenium oxide resistance thermometer were used. One (RuO1) was set at the top part of the mixing chamber and the other (RuO2) was set near the sample.

Chapter 3

Lateral transport

3.1 Quantum Hall effect in lateral transport

Figure 3.1 shows the magnetic field dependence of the in-plane resistance R_{xx} and Hall resistance R_{xy} of superlattice A at 30 mK. From the data of Hall resistance at low field, the sheet density per layer is determined as $n = 2.3 \times 10^{11}$ cm^{-2}/layer. This value is consistent with the period of the Shubnikov-de Hass oscillation in R_{xx}. The mobility of this sample is calculated from R_{xx} at zero magnetic field as $\mu = 6300$ cm^2/V sec which is very small compared with those typically achieved in GaAs/AlGaAs single heterostructures. The small thickness of spacer layer (5 nm) is one of the reasons responsible for the low mobility. The quantum Hall effect (QHE) is observed at filling factors $\nu = 2$ and $\nu = 1$. Note that the quantized value of the Hall resistance is almost 1/100 of the usual value because we have a hundred 2DEGs in parallel.

In Fig.3.2, representative data for other superlattice samples are shown. The in-plane resistance R_{xx} and the Hall resistance R_{xy} of superlattice C and E are depicted. The carrier density per layer and the mobility are determined from the data and they are summarized in table 3.1. As well as superlattice A, the mobility of these superlattices are very low because of thin spacer layer. The quantum Hall effect(QHE) is observed at filling factors $\nu = 2$ and $\nu = 1$ in superlattice C, while no quantized plateau appear in superlattice E. The absence of the quantized plateau in superlattice E can be attributed to its low mobility. Note that small peak structures appear in superlattice C in both R_{xx} and R_{xy} near the center of plateau region. These peak structures become remarkable as temperature is decreased. However, these structures do not seem to be intrinsic feature of superlattices, because they exist only in the Hall bar-shaped sample but not in the van der Pauw-type sample. While the origin of these structures has not identified yet, we suspect that

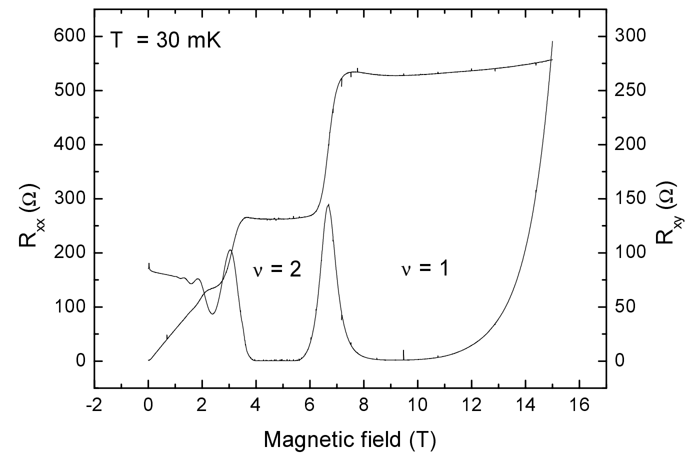

Figure 3.1: The magnetic field dependence of the in-plane resistance R_{xx} and the Hall resistance R_{xy} at 30 mK. The QHE at filling factor $\nu = 1$ and 2 are observed.

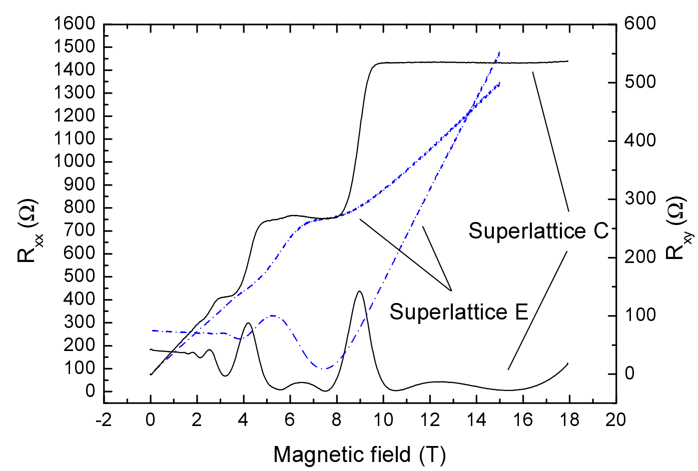

Figure 3.2: The magnetic field dependence of the in-plane resistance R_{xx} and the Hall resistance R_{xy} in superlattice C and E are shown. The data for sample C was taken at 40 mK and that for sample C was taken at 1.5 K.

Superlattice	Barrier width (nm)	Carrier density (10^{11} cm^{-2})	Mobility (cm^2/V sec)
A	15	2.3	6300
C	10	3.1	8200
E	6	3.6	4000

Table 3.1: The sheet carrier density per layer and the mobility of superlattice A, C and E.

these structures might arise from the incompleteness of the Ohmic contact in the Hall bar-shaped sample. Because good Hall bar-shaped samples are not achieved for superlattice C, the Hall bar sample of superlattice A is extensively investigated. In the following, we mainly discuss about the result of superlattice A.

In Fig.3.3, the temperature dependence of R_{xx} at filling factor $\nu = 2$ is plotted. R_{xx} decreases rapidly with decreasing temperature and tends to be constant below 200 mK. In a quantum Hall state, the Fermi energy lies in the localized states between two Landau subbands. Dissipative transport occur at finite temperatures by thermal activation, giving rise to an Arrhenius-type temperature dependence of the resistance,

$$R_{xx} \propto \exp\left(-\frac{E_\mathrm{a}}{k_\mathrm{B}T}\right). \tag{3.1}$$

The activation energy at $\nu = 2$ in the temperature dependence of R_{xx} is obtained by fitting the data as $E_\mathrm{a} = 1.0 \pm 0.1$ K, which is much smaller than $\hbar\omega_\mathrm{c}/2$. Similar observation was reported earlier by Störmer *et al* [11]. This is in contrast to the case of the conventional QHE in single layer 2DEGs where the activation energy in the temperature dependence of R_{xx} is comparable to half the Landau level spacing $\hbar\omega_\mathrm{c}/2$ [28]. It should be noted that although the Landau subband dispersion due to the interlayer transfer widens the central band of the extended states and changes the above quantity to $\hbar\omega_\mathrm{c}/2 - 2t$, the band width $4t = 0.12$ meV for the present sample is too small to account for the observed small value of the activation energy.

This weak temperature dependence is discussed by Störmer *et al.* in terms of depletion layers. Their argument goes as follows. Due to the pinning of the Fermi level, several layers at the top and bottom of the superlattice may be depleted. The transition from completely filled layers to the completely empty layers is not abrupt, but there exist intermediate layers, which are only partially filled. In the case of the in-plane resistance measurement, resistance of these partially filled layers are also measured in parallel. So the weak

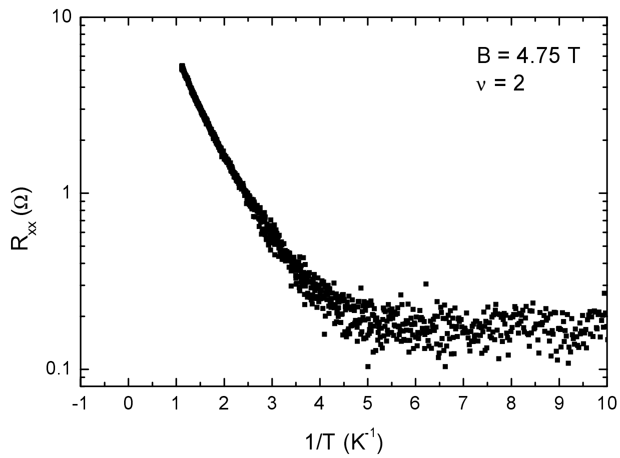

Figure 3.3: The temperature dependence of R_{xx} at $\nu = 2$. R_{xx} decreases rapidly with decreasing temperature and tends to be constant below 200 mK.

temperature dependence of R_{xx} might be associated with the temperature dependence of these partially filled layers.

Another possible source of the weak temperature dependence might be attributed to the low quality of the sample. According to the self-consistent Born approximation, the mobility $\mu = 6300$ cm^2/V sec leads to the width of the Landau subband $\Gamma = 3.8$ meV at $\nu = 2$ ($B = 4.75$ T), which is comparable to the Landau level separation $\hbar\omega_c/2 = 4.1$ meV. This means that there are many localized states at the Fermi level, even though the Fermi level lies between two Landau subbands. Therefore, the relevant process might not be the thermal excitation to the extended states at the center of the Landau subband, but the hopping among these localized states. Though it is difficult to estimate, the relevant activation energy for the latter process can be much smaller than $\hbar\omega_c/2$. Such a small temperature dependence is also reported [29] in the single layer 2DEG at the InGaAs/InP heterostructure with mobility $\mu = 33000$ cm^2/V sec and carrier density $n = 4.5 \times 10^{11}$ cm^{-2}. The temperature dependence of σ_{xx} at $\nu = 3$, 4 and 6 are explained in terms of variable range hopping in the tail of Landau subband [30]. The diagonal conductivity σ_{xx} is expressed as

$$\sigma_{xx} \propto \frac{1}{T} \exp\left[-\left(\frac{T_0}{T}\right)^{1/2}\right], \quad k_B T_0 = \frac{1}{D(E_F) l_B^2}, \tag{3.2}$$

in the model. By fitting the model to the data of temperature dependence of R_{xx}, we obtain the density of states at the Fermi level $D(E_\mathrm{F})$. Figure 3.4 shows their experimental result. The theoretical curve fits the data points, and the values of T_0 obtained from the slopes become $T_0 = 11$, 70 and 7.8 K. However, even the largest value of T_0 ($= 70$ K for $\nu = 4$) gives a value of $D(E_\mathrm{F})$ much larger than the density of states at zero magnetic field $m^*/\pi\hbar^2$. Because the Fermi energy resides in the center of the Landau subgap, one would expect $D(E_\mathrm{F})$ to be much smaller than $m^*/\pi\hbar^2$. Our data gives $T_0 \sim$ 20 K, which also leads to an unreasonable value of $D(E_\mathrm{F})$. To the best of our knowledge, this fundamental inconsistency in the interpretation of weak temperature dependence in the single layer 2DEG has not been solved yet.

As described later in section 4.2, the vertical conductance G_{zz} shows a similar temperature dependence above 200 mK. G_{zz} follows an Arrhenius-type temperature dependence with $E_\mathrm{a}^\mathrm{vertical} = 0.95 \pm 0.05$K. Contrary to the lateral transport, the partially depleted layers as discussed by Stömer *et al.*, even if they exist, should not affect the temperature dependence of G_{zz}, because they are connected with the superlattice in series for the vertical transport measurement. Therefore the activation energy in the vertical transport should be related to the characteristic energy for the hopping conduction. The fact that the lateral and the vertical transport show similar temperature dependences with the same characteristic energy seem to suggest that they are both governed by the same hopping process among the localized states.

3.2 The QHS-HI transition in semiconductor superlattice

The problem of the quantum Hall state (QHS) to Hall insulator (HI) transition in a three-dimensional (3D) system is discussed in this section. As described in section 1.5, the critical exponent in the multilayered system is expected to differ from that in the strictly 2D system. In order to determine the critical exponent experimentally, the transition from QHS to HI was investigated. Experiments were performed by using Hall bar-shaped samples of superlattice A and superlattice C, in which the interlayer transfer integral t are different. Though magnetic field was applied up to 18 T, the critical magnetic field for superlattice C is out of the reach of the present experimental setup because of large carrier density in superlattice C. In the following of this section, the experimental results of superlattice A are discussed.

Figure 3.5 shows the magnetic field dependence of the diagonal sheet resistivity ρ_{xx} of sample A up to 18 T at $T = 147$, 208, 379, 490 and 566 mK.

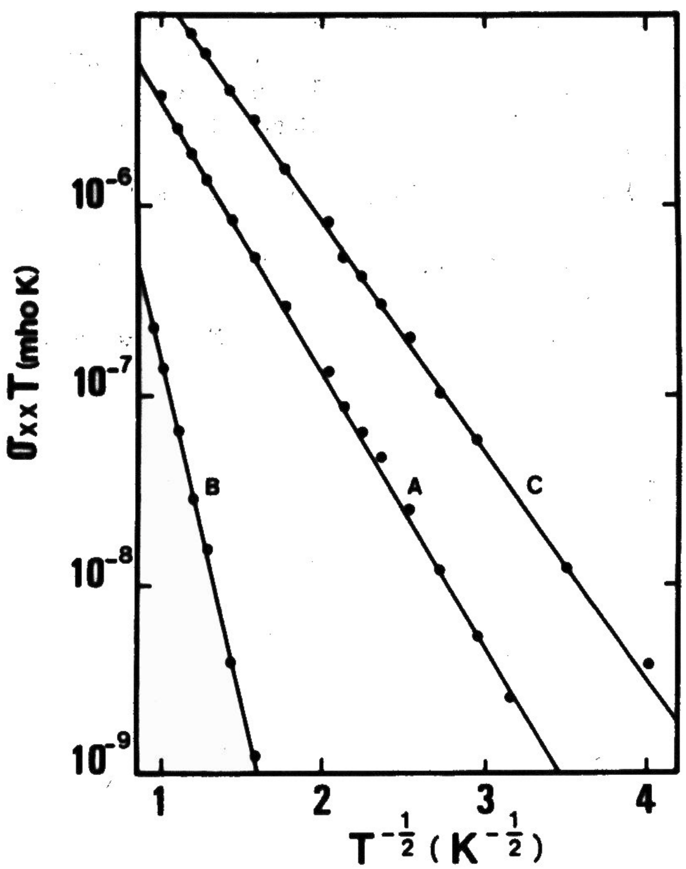

Figure 3.4: Experimental data by Briggs *et al* [29]. Temperature dependence of σ_{xx} at the minima (A) $\nu = 6$, (B) $\nu = 4$ and (C) $\nu = 3$.

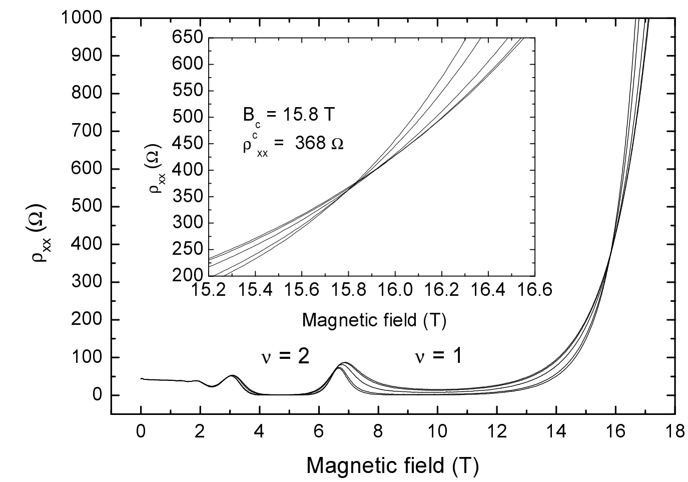

Figure 3.5: The magnetic field dependence of the in-plane sheet resistivity ρ_{xx} at $T = 144$, 208, 379, 490 and 566 mK. The same data around the QHS-HI transition is enlarged in the inset. All the curves with different temperatures cross at a same point.

All the traces with different temperatures cross at magnetic field $B_{\mathrm{c}} = 15.8$ T as shown in the inset of Fig.3.5. When magnetic field is smaller than B_{c}, ρ_{xx} decreases as temperature is decreased. On the other hand, ρ_{xx} increases with decreasing temperature at magnetic field above B_{c}. This behavior is same as the QHS-HI transitions in single layer 2DEGs. The critical value of the diagonal resistivity ρ^{c}_{xx} at the magnetic field B_{c} is 368 Ω. Because the system consists of a hundred 2D layers in parallel, ρ^{c}_{xx} is almost 1/100 of ρ^{c}_{xx} reported in conventional single layer 2DEGs and is on the order of 0.01 h/e^2.

As similar to the 2D QHS-HI transition, temperature scaling analysis was performed. In Fig.3.6, the data of temperature dependence of ρ_{xx} at fixed magnetic fields near B_{c} is plotted. It shows ρ_{xx} as a function of the scaling variable $|B - B_{\mathrm{c}}|/T^{\kappa}$, where κ is used as a fitting parameter so that all the data is scaled on a single curve. The upper curve corresponds to the data for $B > B_{\mathrm{c}}$, while the lower for $B < B_{\mathrm{c}}$. We obtain $\kappa = 0.30 \pm 0.05$. The error in the value of critical exponent κ comes mainly from the uncertainty in the thermometry in high magnetic fields. It is rather difficult to obtain temperature precisely in magnetic field in this temperature range. The calibration of the thermometer in magnetic field is mentioned in section 2.2. The obtained value of κ is slightly smaller than those reported for single

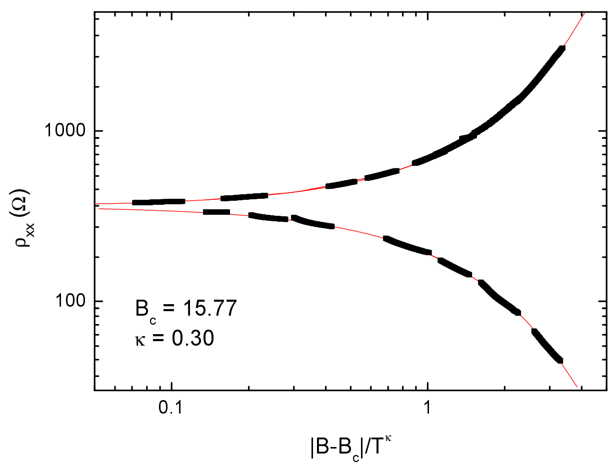

Figure 3.6: ρ_{xx} data taken by varying temperature at fixed magnetic fields around B_c is plotted against the scaling variable $|B - B_\mathrm{c}|/T^\kappa$.

layer 2DEGs. κ is related to the critical exponent μ by $\kappa = 1/z\mu$,where z is the dynamical exponent. As the dynamical exponent z also depends on the dimension of the system, we cannot compare the experimentally obtained κ to the theoretically obtained[10] critical exponent μ directly. In order to discuss the effect of dimensionality, the values of z and μ should be determined independently. The electric field scaling experiment will make it possible to determine z and μ separately.

Note that the magnetic field dependent traces of ρ_{xx} for different temperatures cross at a single point as shown in Fig.3.5. This is contradictory to the theoretical predictions. In the 3D systems, the mobility edge at the center of the Landau subband has widened to a band with its width $4t$. When the Fermi level resides in these extended states, the corresponding wave functions at the Fermi level are three-dimensionally extended, leading to almost temperature independent metallic diagonal resistivity. According to Ohtsuki *et al.*, the states only slightly away from the center of the Landau subband that are localized for $t = 0$ must rapidly become delocalized with a small amount of the interlayer transfer t. The mobility edge moves as $E_\mathrm{c}/\Gamma \sim (2t/\Gamma)^{1/4}$, where E_c is the mobility edge measured from the center of the Landau subband and Γ is the half width of disorder-broadened Landau subband. By using $\Gamma \sim 6.9$ meV at 15.8 T, the energy of the mobility edge is calculated as 2.1 meV corresponding to the range of magnetic field $\Delta B \sim 2.4$ T around B_c. The experimental result does not show metallic temperature dependence in such wide range of magnetic field. The absence of the width of the temperature independent metallic region might be attributed to small value of $2t/\Gamma = 0.087$ at $B = 15.8$ T which is actually out of the reliable range of the numerical study ($2t/\Gamma = 0.15$ to 0.90). The transfer integral of the present sample might be so small that each layer might behave as an independent 2DEG.

The following experimental result can be understood in this line. The QHS-HI transition experiments were performed in tilted magnetic fields. As magnetic field is tilted from the normal direction, the interlayer transfer integral $\tilde{t}_{0,0}$ between the states in adjacent layers in the 0-th Landau level decreases[31, 32] as

$$\tilde{t}_{0,0} = t \exp\left[-\left(\frac{a}{2l_{B_\perp}} \tan\theta \right)^2 \right], \tag{3.3}$$

where θ is the tilt angle measured from the normal direction, $l_{B_\perp}$ is the magnetic length associated with the perpendicular component of the magnetic field, a is the interlayer spacing and t is the transfer integral at $\theta = 0$. As the reduction of the interlayer transfer makes the system two-dimensional, the magnetic field dependence or the temperature dependence of ρ_{xx} near the transition region is expected to change as a the function of tilt angle.

Figure 3.7 shows the magnetic field dependence of ρ_{xx} at $T = 210$ mK and 570 mK for $\theta = 0°$, $10°$ and $20°$. The horizontal axis is the perpendicular component of magnetic field. Neither the critical magnetic field B_c nor the temperature dependence of ρ_{xx} changes as the magnetic field is tilted. Small discrepancy between the curve for $\theta = 0°$ and curves for $\theta = 10°$ and $20°$ can be explained by the errors of field tilt angle θ. This result implies that each layer behave as an independent 2DEG and no 3D extended states exists at the center of Landau levels.

To summarize the discussion in this section, the QHS-HI transition in weakly coupled multilayered quantum Hall system was investigated experimentally. The value of exponent $\kappa = 0.30 \pm 0.5$ in this system is smaller than that for a single layer 2DEG. The absence of the metallic region near the critical field and the insensitivity to the in-plane magnetic field may suggest that the present sample behaves as a stack of individual 2DEGs. Further experiments with larger interlayer transfer t will be required to reveal the nature of the 2D-3D dimensionality crossover for the Anderson localization in high magnetic field.

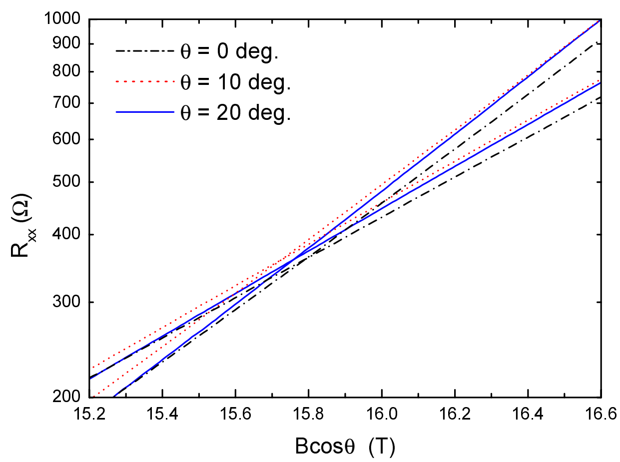

Figure 3.7: The magnetic field dependence of ρ_{xx} for several tilt angles. The critical magnetic field B_{c} does not change as the magnetic field is tilted.

Chapter 4

Chiral surface state

The experimental results of the vertical transport in a GaAs/AlGaAs semiconductor superlattice in the quantum Hall regime is described in this chapter. Sample size dependence, temperature dependence, non-Ohmicity and the effect of the transverse magnetic field in the vertical transport of superlattice A are mainly discussed. Other superlattices (B and C) show qualitatively similar result as superlattice A. Comparison between superlattices are descried in section 4.5.

4.1 Size dependence of vertical conductance

In Fig.4.1(b), the magnetic field dependence of the out-of-plane resistance R_{zz} of superlattice A is plotted for three mesas of different sizes. The sample sizes are 50×50 μm^2, 100×100 μm^2 and 200×200 μm^2 from top to bottom. In the magnetic field range where the lateral transport exhibits the quantum Hall effect (QHE), the out-of-plane resistance R_{zz} becomes maximum. In the inset of Fig.4.1(b), the size dependence of the out-of-plane conductance $G_{zz} = 1/R_{zz}$ at $\nu = 2$ is plotted. G_{zz} is not proportional to mesa cross-section S but proportional to mesa perimeter C, suggesting that the vertical transport at $\nu = 2$ is dominated by the surface states as reported by Druist *et al* [22].

The edge state in each layer is expected to have a finite width due to the screening effect[33]. According to Takaoka *et al.*, who have investigated the width of the edge states by magnetocapacitance measurement in single layer 2DEGs[34], the width of edge states at $\nu = 2$ is about 1 μm. Though it is impossible to obtain the thickness of the chiral surface state from the present experiments, the fact that G_{zz} is scaled by the nominal value of mesa perimeter C indicates that the thickness of the chiral surface state is

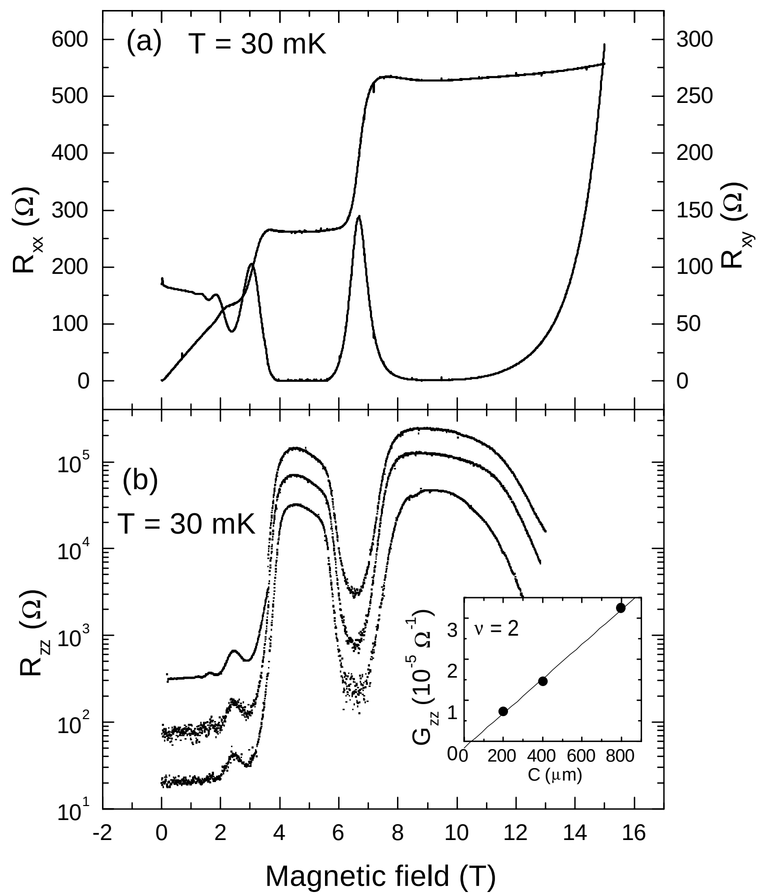

Figure 4.1: (a) Magnetic field dependence of the in-plane resistance R_{xx} and the Hall resistance R_{xy}. (b) Magnetic field dependence of the out-of-plane resistance R_{zz}. The sample sizes are 50 $\times$ 50 μm^2, 100 $\times$ 100 μm^2 and 200 $\times$ 200 μm^2 from top to bottom. The inset shows the size dependence of the out-of-plane conductance G_{zz} at $\nu = 2$.

sufficiently small compared to the sample size. The vertical conductance of smaller samples might deviate from the perimeter scaling due to the finite thickness of surface states.

A few different regimes exist for the transport properties of the chiral surface state [18, 19, 21]. Provided that the sample is smaller than the phase coherence length, an electron can circumnavigate the sample coherently. On the other hand, if the sample is larger than phase coherent length, the whole sample is regarded as a network of phase coherent patches. There are some important length scales that characterize these regimes. One is the phase coherence length in the z-direction $L_\phi = \sqrt{D\tau_\phi}$, where D is the diffusion constant along the z-direction and τ_ϕ is the phase coherence time. If the sample height L along the z-direction is shorter than L_ϕ, an electron can travel from one electrode to the other coherently. The sample for $L < L_\phi$ is called coherent regime and $L > L_\phi$ is called incoherent regime. The coherent regime is further divided to three different regimes [19]. Three different regimes of the phase coherent transport are summarized in Fig.4.2. Here, ξ_0 is the quasi-one-dimensional localization length, $L_1 \sim \sqrt{DC/v}$ is the distance that an electron diffuses in the z-direction during the time taken to circumnavigate the sample, C is the sample perimeter and v is the velocity along the chiral direction. The localization length ξ_0 is expected to be proportional to the 1D conductivity, $\xi_0 \sim \sigma C$. If the sample height L is longer than the 1D localization length ξ_0, the sample becomes 1D insulator. In the case of $L_1 < L < \xi_0$, an electron can circumnavigate the sample for many times during it travels from one electrode to the other. This regime is referred as 1D metal. If the sample height L is shorter than L_1, an electron can travel from one electrode to the other before it circumnavigate the sample. This regime is called as 2D metal. The features of the conductance fluctuation are different from these regimes. By investigating the conductance fluctuation experimentally, one can determine to which regime the sample belongs.

However, it is rather difficult to distinguish the intrinsic conductance fluctuation from the experimental noise. In order to obtain reliable data, improvement of the signal to noise (S/N) ratio is required. Though it is difficult to mention about the phase coherence length from the present experiment, it is not likely that the phase coherence length is longer than $L \sim 2.5\mu$m. We speculate that our sample belongs to the phase incoherent regime.

4.2 Temperature dependence

The temperature dependence of the out-of-plane conductance at $\nu = 2$ is shown in Fig.4.3. This result is also qualitatively similar to the previous

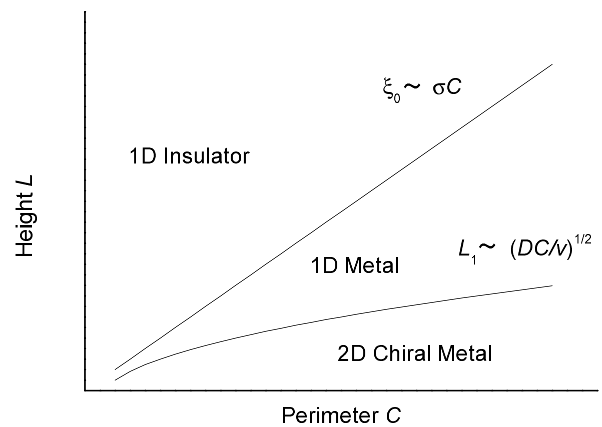

Figure 4.2: Three different regimes of the phase coherent transport of the chiral surface state with height L and perimeter C.

work by Druist *et al* [22]. The upper panel (a) shows the two-dimensional (2D) conductivity scaled by mesa perimeter C and the lower panel (b) shows the three-dimensional (3D) conductivity scaled by mesa cross-section S. Here $L = 100 \times 25$ nm is the total thickness of the superlattice part. For these measurements, the excitation current was kept less than 3 nA to avoid electron heating. As the temperature is decreased, G_{zz} decreases rapidly following an Arrhenius-type temperature dependence, but it becomes nearly constant below 100 mK. As seen in Fig.4.3(a), the constant values of the conductivity below 100 mK are the same for the three samples when scaled by mesa perimeter C. This indicates that there is a conductive sheath at the side face of the mesa, which remains "metallic" at low temperatures. The measured temperature independent 2D sheet conductivity is $\sigma_{zz}^{\mathrm{2D}}(\nu = 2) = 3 \times 10^{-3} e^2/h$ which is much smaller than e^2/h . This value is about twice the value reported by Druist *et al* [22]. This difference may be understood in the following sense. According to the theory by Balents and Fisher [16], the sheet conductivity at $\nu = N$ is given by

$$\sigma_{zz}^{2D}(\nu = N) = N \frac{e^2 t^2 \tau a}{2\pi \hbar^3 v}, \tag{4.1}$$

where t is the interlayer transfer integral, τ is the elastic scattering time, a is the interlayer spacing and v is the electron velocity of the edge channel. This equation contains two unknown parameters τ and v, whose values are

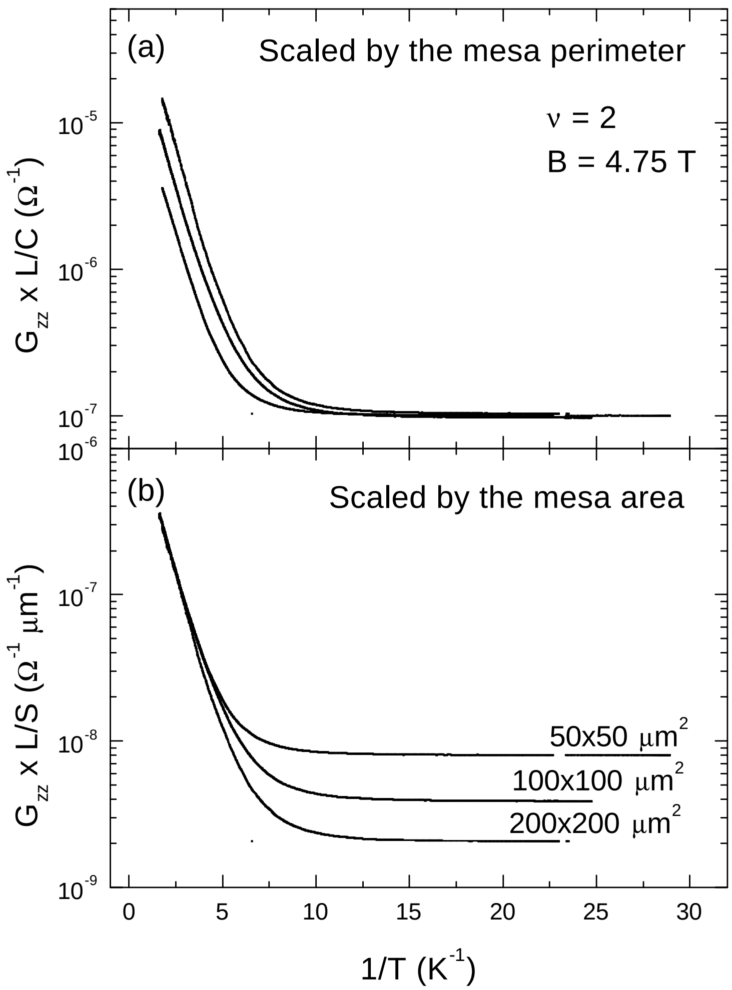

Figure 4.3: Temperature dependence of G_{zz}. The vertical axis is scaled by (a) mesa perimeter and by (b) mesa area.

As temperature is increased, the 2D conductivity curves scaled by mesa perimeter start to deviate from each other. Above 200 mK, the conductance data for different mesa sizes are reduced to a single curve by scaling them by mesa cross-section. This indicates that the dominant vertical transport at these high temperatures is through the bulk of the mesas. In the quantum Hall system, if the spatial correlation between different layers is small, the wave function cannot extend over many layers along the z-direction. The vertical transport through the bulk states can only occur at finite temperatures by thermal activation. The measured G_{zz} in the high-temperature region shows an Arrhenius-type temperature dependence,

$$G_{zz} \propto \exp\left(-E_{\mathrm{a}}/k_{\mathrm{B}}T\right), \tag{4.2}$$

with the activation energy $E_{\mathrm{a}} = 0.95 \pm 0.05$ K which is much smaller than $\hbar\omega_{\mathrm{c}}/2 = 4.1$ meV $= 48$ K. As discussed in section 3.1, the half width of the disorder-broadened Landau subband $\Gamma = 3.8$ meV is so large as to be comparable with $\hbar\omega_{\mathrm{c}}/2 = 4.1$ meV indicating that many localized states exist at the Fermi level. As described in section 3.1, the hopping among these localized states might be responsible for the conduction at finite temperature in the vertical transport as well as in the lateral transport. Therefore the small value of the slope of the G_{zz} versus T curve in the bulk transport regime is related to the characteristic energy for the hopping conduction, which might be smaller than $\hbar\omega_{\mathrm{c}}/2$.

In principle, it should be possible to extract the temperature dependence of the surface conductivity from the total conductivity by subtracting the contribution of the bulk transport. Such analysis was performed by Kuraguchi *et al* [35]. The difference of the conductivity normalized by cross-section is plotted against temperature in Fig.4.4. The upper curve shows the difference of the conductivity between 50×50 μm^2 mesa and 200×200 μm^2 mesa the lower curve corresponds to the difference between 50×50 μm^2 mesa and 100×100 μm^2 mesa. As the bulk contribution of the conductivity is subtracted, the remainder is considered as the contribution from the surface transport. The remaining conductivity increases as the temperature is increased above 150 mK in the upper curve. The qualitatively similar result is reported by Kuraguchi *et al.* They discussed this temperature dependence in terms of the mixing of the edge states and bulk states. As temperature is increased, edge states begin to hybridize with the bulk states widening the width of the edge states. This causes the increase of remaining conductivity after the subtraction. Our result of the upper curve in Fig.4.4 seems consistent with this line of interpretation qualitatively.

However, the subtraction of the conductivity between 50×50 μm^2 mesa and 100×100 μm^2 mesa gives an opposite result as shown in the lower trace of Fig.4.4. This is the consequence of the over-subtraction. Although the nominal value of sample cross-section was used in the above analysis, the cross-section of the actual sample is expected to be a little smaller than

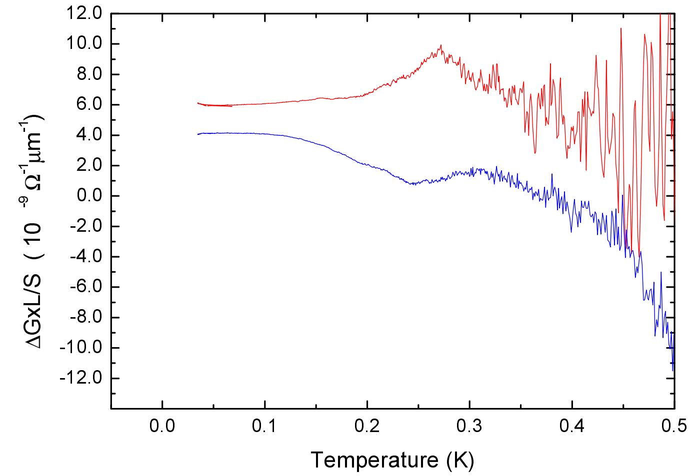

Figure 4.4: The difference of the conductivity normalized by mesa cross-sections. The upper curve shows the difference of the conductivity between 50×50 μm^2 mesa and 200×200 μm^2 mesa, and the lower curve corresponds to the difference between 50×50 μm^2 mesa and 100×100 μm^2 mesa.

the nominal value because of the presence of depletion layers and errors of the sample fabrication. It is difficult to define the cross-section of the mesas precisely. Note that the vertical axis in Fig.4.3 is plotted in log-scale. Because the bulk conductivity shows very strong temperature dependence, the small ambiguity of the mesa cross-section can make the present analysis unreliable. The temperature dependence in the lower curve in Fig.4.4 may reflect the remaining bulk contribution due to the incomplete subtraction.

4.3 Current-voltage characteristics

Next, we turn our attention to the non-Ohmicity in the vertical transport in the quantum Hall regime. The experiments were carried out by measuring the differential resistance $\mathrm{d}V/\mathrm{d}I$ as a function of the dc bias current. In Fig.4.5, the differential conductance $\mathrm{d}I/\mathrm{d}V$ is plotted against the voltage calculated from the data. Data for three samples with different sizes are shown. The temperature was kept at 30 mK during the measurements. As in Fig.4.3, the vertical axis is scaled by mesa perimeter in the upper panel and by mesa cross-section in the lower panel. At voltages below 0.5 mV the differential conductivity scaled by mesa perimeter collapses onto a single curve as seen in Fig.4.5(a). On the other hand, the differential conductivity reduced by mesa cross-section is on a single curve at voltages above 0.7 mV as shown in Fig.4.5(b). Such scaling indicates that the current is carried mainly by the surface states in the low-voltage region but is extended to the bulk of the sample in the high voltage region. It should be noted that the differential conductivity exhibits significant voltage dependence in both low voltage and high voltage region.

Let us first consider the high-voltage region where the current flows mainly through the bulk of the sample. Because the Fermi level resides in the tail part of the Landau subband, the relevant wave functions are highly localized. The conduction occurs via hopping between these localized states near the Fermi level in this regime. The localization length in the z-direction ξ_z is presumably not much greater than the interlayer distance.

Here, let us introduce a simple model to describe the hopping conduction between the localized states in the presence of bias voltage [36]. Assume that a symmetric barrier exists separating the path of current flow. In the absence of bias voltage, the chemical potential μ is practically same at the left and the right of barrier as depicted in Fig.4.6 (dashed line). If the bias voltage U is applied across the barrier, the electrochemical potential is raised to $\mu + eU/2$ in the left side of the barrier and lowered to $\mu - eU/2$ in the right side of the barrier. The bias voltage play a role to reduce (increase) the effective barrier height for the electrons hopping from left to right (from right to left). Then the thermally activated hopping current in the presence of the voltage bias is given by

$$I \propto \exp\left(-\frac{E_{\mathrm{a}}}{k_{\mathrm{B}}T}\right)\sinh\left(\frac{eU/2}{k_{\mathrm{B}}T}\right), \tag{4.3}$$

for $k_{\mathrm{B}}T, eU/2 \ll E_{\mathrm{a}}$. Here, E_{a} is the difference between the maximum of barrier height and the chemical potential μ. In the limit of $eU/2 \ll k_{\mathrm{B}}T$, Ohm's law follows from this expression. When $eU/2$ approaches E_{a}, the above formula is no longer applicable and the voltage dependence will be less steep than the exponential form. The bias-voltage dependence of the differential conductivity shown in Fig.4.5(b) qualitatively agrees with the picture above. This model for hopping conduction is further supported by the following experiment.

The differential conductance $\mathrm{d}I/\mathrm{d}V$ at several temperatures are plotted against the voltage across the superlattice in Fig.4.7. At these temperatures (above 200 mK) the conductance is dominated by bulk transport even at the lowest voltage.

Suppose that the bias voltage V is applied across the superlattice with the thickness along the z-direction L. Assuming that the superlattice contains

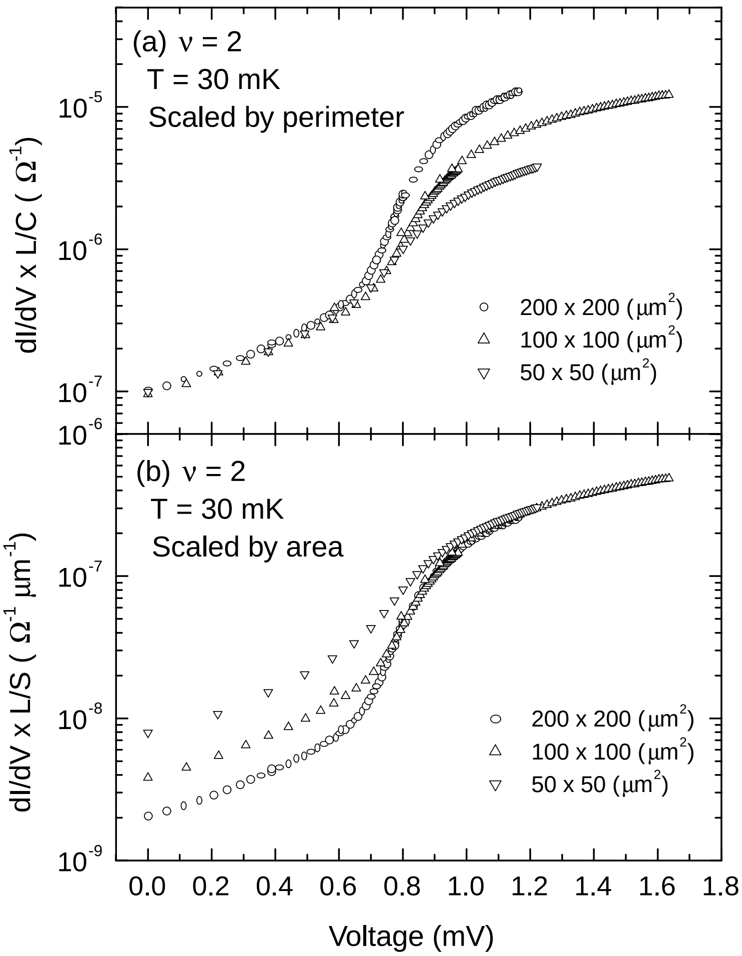

Figure 4.5: Voltage dependence of the differential conductance $\mathrm{d}I/\mathrm{d}V$. The vertical axis is scaled by (a) mesa perimeter and by (b) mesa area.

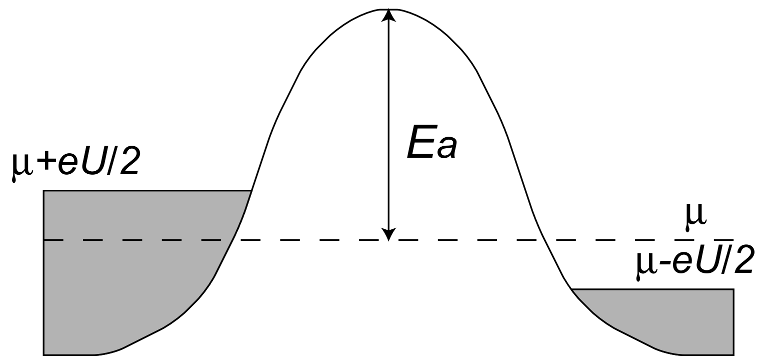

Figure 4.6: A schematic picture of a model for thermally activated hopping conduction in the presence of bias voltage. The voltage plays a role to decrease (increase) the barrier height $eU/2$ for the hopping left to right (right to left).

localized states with its extent ξ_z in series, the voltage drop between each localized state should be $V/(L/\xi_z)$. Replacing U in eq.(4.3) by $V/(L/\xi_z)$, the differential conductance can be written as

$$\frac{\mathrm{d}I}{\mathrm{d}V} \propto \cosh\left(\frac{V}{V_0}\right), \tag{4.4}$$

where $eV_0 = (2L/\xi_z)k_{\mathrm{B}}T$. V_0 is obtained for each temperature by fitting the data in Fig.4.7 by eq.(4.4). Data below 1.0 mV was fitted. The temperature dependence of V_0 is plotted in the inset of Fig.4.7. Then quantity L/ξ_z is estimated from the slope of the V_0 versus T plot as $L/\xi_z \sim 10$. This means that the localization states extend along the z-direction over 10 layers on average. Although such number should not be taken literally, the picture that the localized states extend over a few layers seems reasonable. In the high voltage bulk transport regime, the transport mechanism seems to be explained by the voltage assisted hopping between the localized states at the Fermi level. At the lower temperatures below 200 mK, as decreasing the bias voltage, the bulk differential conductance drops rapidly below the value of the surface conductance. In this regime a bias-voltage-driven crossover from surface transport to bulk transport occurs.

We now consider the behavior in the low voltage region, where the transport current is mostly carried by the surface sheath. As noted earlier, a significant non-Ohmicity is also observed in the low-voltage region. We emphasize that this non-Ohmicity is quite substantial, and it persists down to the lowest voltage of the present experiment. It is noteworthy that the sheet

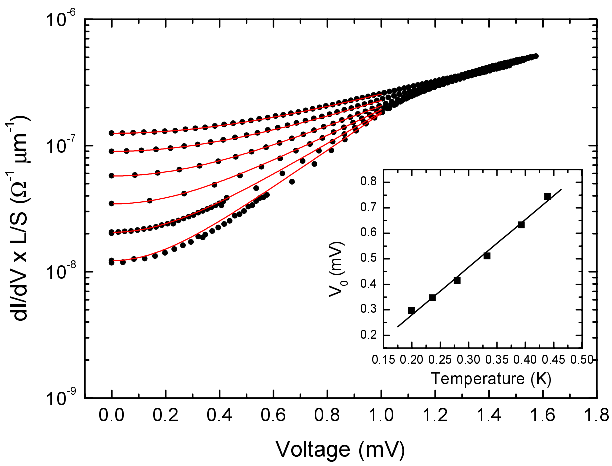

Figure 4.7: The differential conductance $\mathrm{d}I/\mathrm{d}V$ is plotted against the bias voltage V at several temperatures. The temperatures are 440, 390, 330, 280, 340 and 200 mK from top to bottom. The inset shows the temperature dependence of the fitting parameter V_0.

conductance in this region does not exhibit appreciable temperature dependence. So, the non-Ohmicity in the surface transport regime is distinct from the electron heating effect. This non-Ohmicity together with the sheet conductance much less than e^2/h reflects the marginally metallic nature of the chiral surface state. Provided that the phase coherence length is larger than the mesa perimeter C, increasing the ratio L/C will lead to a crossover from metallic behavior to 1D localized behavior [19]. The observed non-Ohmicity may be a type of precursor of this crossover. Although the origin of the non-Ohmicity of the surface transport is not clear at the present stage, we hope that the present work will stimulate theoretical efforts to incorporate the effect of the finite bias voltage in the description of the chiral surface state.

4.4 Transverse magnetoresistance

In this section the effect of in-plane magnetic field on the vertical transport in the quantum Hall regime is discussed.

According to the theory by Chalker and Sondhi [17], the conductance of the chiral surface state along the z-direction in the presence of $B_\parallel$ is given by

$$\sigma_{zz}(B_\parallel) = \frac{\sigma_{zz}(B_\parallel = 0)}{1 + (B_\parallel/B_0)^2}, \tag{4.5}$$

where $B_\parallel$ is the magnetic field component perpendicular to the chiral surface state, $B_0 = \Phi_0/al_{\rm el}$, $\Phi_0 = h/e$, a is the interlayer spacing and $l_{\rm el}$ is the elastic scattering length in the chiral surface state. This is essentially a semi-classical (Drude-like) magnetoresistance of the chiral surface state. Consider a chiral surface state in which the edge states in adjacent layers are coupled with transfer integral t and are separated with spacing a. We take the x-axis in the chiral direction and the z-axis in the interlayer direction on the chiral surface state as shown in Fig.4.8. The dispersion relation can be written in the following form,

$$\varepsilon(k_x, k_z) = \hbar v k_x - 2t\cos(k_z a), \quad k_x > 0. \tag{4.6}$$

Here, v is the electron velocity in the x-direction. Because of chirality in the x-direction, there is only $k_x > 0$ branch in the dispersion relation. A schematic picture of the Fermi surface is shown in Fig.4.8. The Lorentz force arising from the transverse magnetic field $B_\parallel$ will sweep electrons across the Brillouin zone in the z-direction. Correspondingly, electrons follow a snaking path in real space as shown in Fig.4.8. This semi-classical orbital motion of electron causes the transverse magnetoresistance.

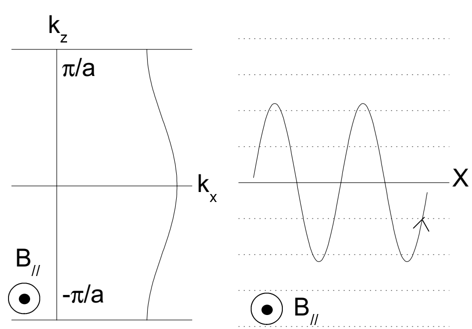

Figure 4.8: A schematic picture of the Fermi surface of the chiral metal and trajectory of electrons in real space in the presence of transverse magnetic field.

The magnetotransport can be appropriately treated in the framework of the Boltzmann equation because of the absence of the quantum interference effect. As electrons move in the x-direction with velocity v, the equation of motion in the presence of transverse magnetic field $B_\parallel$ is written in the following form,

$$\hbar \frac{\mathrm{d}k_z}{\mathrm{d}t} = evB_\parallel. \tag{4.7}$$

Then the band velocity along the z-direction is calculated as

$$v_z(t) = \frac{1}{\hbar}\frac{\partial \varepsilon}{\partial k_z} = \frac{2ta}{\hbar}\sin\left[ak_z(t)\right] = \frac{2ta}{\hbar}\sin\left[ak_z(0) + \tilde{\omega}t\right], \tag{4.8}$$

where $\tilde{\omega} = evB_\parallel a/\hbar$. By putting $v_z(t)$ into the Boltzmann equation, one obtains the out-of-plane conductivity $\sigma_{zz}(B_\parallel)$.

$$\begin{aligned}
\sigma_{zz}(B_\parallel) &= \frac{e^2}{(2\pi)^2}\int\int \mathrm{d}k_x \mathrm{d}k_z \left[\left(-\frac{\partial f_0}{\partial \varepsilon}\right)\int_0^\infty \mathrm{d}t\ v_z(0)v_z(t)e^{-t/\tau}\right] && (4.9)\\
&\sim \frac{e^2}{(2\pi)^2}\int \frac{\mathrm{d}\varepsilon}{\hbar v}\left(-\frac{\partial f_0}{\partial \varepsilon}\right)\int \mathrm{d}k_z \left[\int_0^\infty \mathrm{d}t\ v_z(0)v_z(t)e^{-t/\tau}\right] && (4.10)\\
&= \frac{\sigma_{zz}(B_\parallel = 0)}{1+(\tilde{\omega}\tau)^2} && (4.11)
\end{aligned}$$

Note that the magnetoresistance in eq.(4.5) arises only from the chiral surface state perpendicular to $B_\parallel$. The conductance of the surface state parallel to $B_\parallel$ is not affected by $B_\parallel$ in this model.

Figure 4.9 shows the results of R_{zz} measurement under tilted magnetic fields. The tilt angle θ was defined with respect to the direction normal to the layer plane as shown in the inset of Fig.4.9. The horizontal axis is the normal component of the magnetic field $B_\perp = B\cos\theta$. It is seen that the peak value of R_{zz} at $\nu = 2$ increases with increasing tilt angle θ, or with increasing in-plane field component $B_\parallel$. Note that the magnetic field is tilted so that $B_\parallel$ is parallel to the edge of the square sample. There are two inequivalent kinds of mesa-sides in this configuration. Two sides are normal to $B_\parallel$ and the other two sides are parallel to $B_\parallel$. In Fig.4.10, $G_{zz} = 1/R_{zz}$ at $B_\perp = 4.75$ T is plotted by solid squares against $B_\parallel$. The open diamond points in Fig.4.10 represent the similar data for the field tilt along the diagonal direction. In this case, all the four mesa-sides are equivalent with respect to the in-plane magnetic field. As seen in Fig.4.10, the vertical conductance $G_{zz}(B_\parallel)$ is almost the same in both configurations. This result shows that the transverse magnetoresistance of the chiral surface state is insensitive to the direction of the in-plane magnetic field. Druist *et al.* also report [37] that the transverse magnetoresistance is insensitive to the direction of in-plane magnetic field $B_\parallel$ by using rectangular shaped mesas.

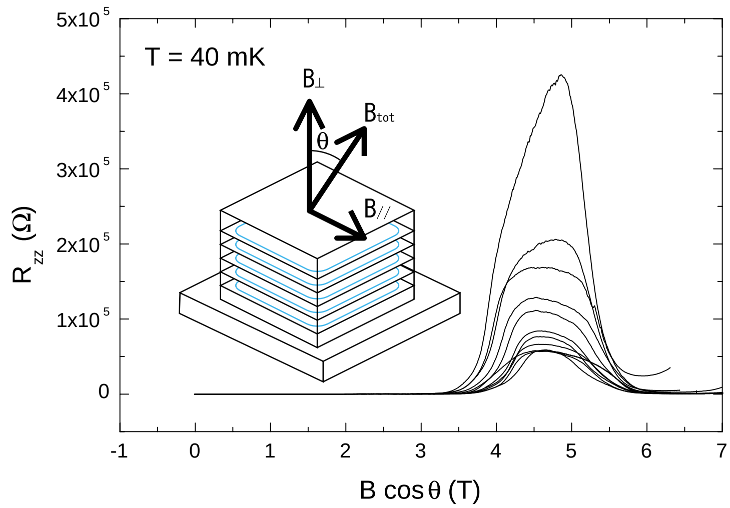

Figure 4.9: Magnetic field dependence of R_{zz} for different tilt angles of the magnetic field at $T = 40$ mK. The tilt angle $\theta = 0°, 10°, 15°, 18°, 25°, 28°, 33°, 38°, 44°, 50°$ and $61°$ from bottom to top. The horizontal axis is the magnetic field component normal to the layer plane, $B_\perp = B\cos\theta$.

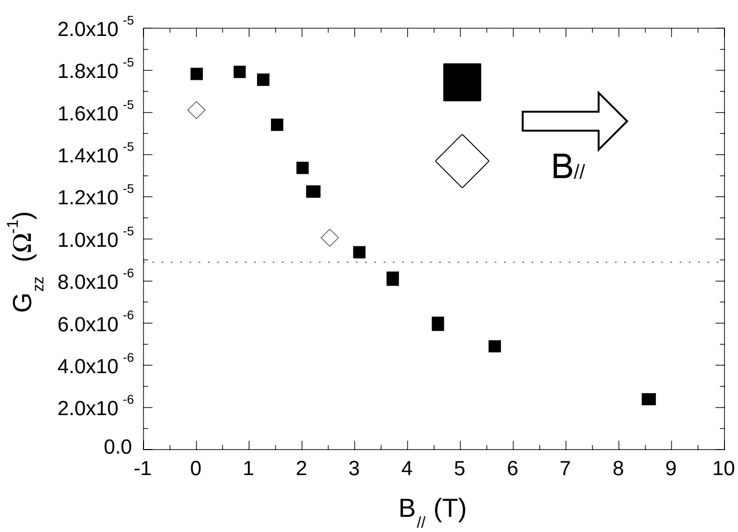

Figure 4.10: $G_{zz} = 1/R_{zz}$ at $B_\perp = 4.75$ T is plotted by solid squares against $B_\parallel$. The open diamond points represent the similar data for the field tilt along the diagonal direction.

Suppose that the in-plane field $B_\parallel$ is applied in the configuration of black square in the inset of Fig.4.10. In the limit of $B_\parallel \to \infty$, the total conductance $G_{zz}(B_\parallel = \infty)$ should approach $G_{zz}(B_\parallel = 0)/2$ according to the model described above, because the conductance of two faces which are parallel to $B_\parallel$ is not changed by $B_\parallel$. However, the experimental data in Fig.4.10 (solid squares) shows that G_{zz} becomes much smaller than $G_{zz}(B_\parallel = 0)/2$ at large $B_\parallel$. Together with the above mentioned insensitivity to the in-plane field direction, this result cannot be explained within the framework of the theory by Chalker and Sondhi.

One may attribute the insensitivity to the $B_\parallel$ direction to a possible irregularity of the side faces. If the side faces of the mesa are not flat but winding in a zigzag pattern on the scale of $l_{\rm el}$, the $B_\parallel$-direction dependence of G_{zz} would be smeared out. However, this scenario can be ruled out. The contribution to the total conductivity from the portion of the side faces which make large angle with $B_\parallel$ goes to zero as $B_\parallel \to \infty$ according to eq.(4.5). So, the ratio $G_{zz}(B_\parallel = \infty)/G_{zz}(B_\parallel = 0)$ gives a measure of the fraction of the side faces which are almost parallel to $B_\parallel$. The smallness of this value ($G_{zz}(B_\parallel)/G_{zz}(0) \sim 0.11$ at $B_\parallel = 9T$) seen in Fig.4.10 makes it unlikely that it can be explained by eq.(4.5) combined with the side face roughness. Thus, at least a substantial part of the observed large magnetoresistance has to be attributed to some mechanisms other than the semi-classical magnetoresistance given by eq.(4.5).

A candidate for an alternative mechanism is the reduction of the interlayer transfer integral by in-plane magnetic field [31, 32]. When the magnetic field is tilted from the direction normal to the layer plane, the interlayer transfer integral between the bulk states in adjacent layers given by

$$\begin{aligned} \tilde{t}_{N,N'} &= t\int_{-\infty}^{\infty} \mathrm{d}x \phi_{N'}\left(x - \frac{a}{2l_{B_\perp}}\tan\theta\right)\phi_N\left(x + \frac{a}{2l_{B_\perp}}\tan\theta\right) \quad (4.12)\\ &= t\sqrt{\frac{2^{N'}N!}{2^N N'!}}\exp\left[-\left(\frac{a}{2l_{B_\perp}}\tan\theta\right)^2\right]\left(-\frac{a}{2l_{B_\perp}}\tan\theta\right)^{N-N'} \\ &\quad \times L_N^{N-N'}\left[2\left(\frac{a}{2l_{B_\perp}}\tan\theta\right)^2\right], \quad (4.13)\end{aligned}$$

where N and N' are the Landau level indices, $l_{B_\perp}$ is the magnetic length associated with the out-of-plane field component $B_\perp$, $\phi_N(x)$ is the eigenfunction of a harmonic oscillator and $L_N^{N-N'}(x)$ is a generalized Laguerre polynomial. The effective interlayer transfer integral $\tilde{t}_{N,N'}$ decreases with increasing tilt angle θ. The vertical conductivity is expected to be proportional to $\tilde{t}^2_{N,N'}$. The same data as in Fig.4.10 (the vertical conductance at $\nu = 2$) is plotted

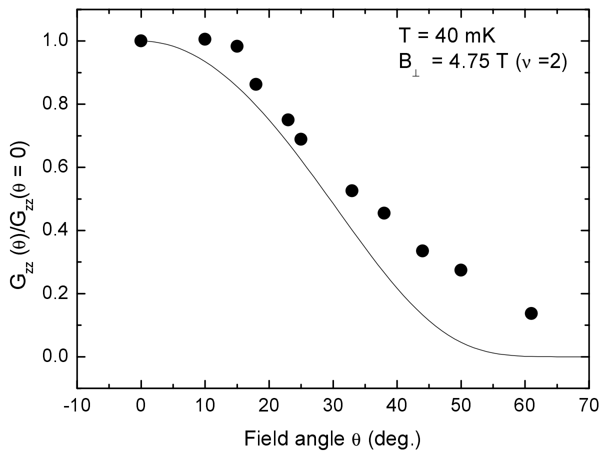

Figure 4.11: The vertical conductance at $\nu = 2$ is plotted against the filed tilt angle θ. The vertical axis is normalized by $G_{zz}(\theta = 0)$. The solid line shows $\left(\tilde{t}_{0,0}/t\right)^2$ with the parameters $l_{B_\perp} = 12$ nm and $a = 25$ nm.

against the filed tilt angle θ in Fig.4.11. The vertical axis is normalized by $G_{zz}(\theta = 0)$. The solid curve in Fig.4.11 represents $\left(\tilde{t}_{0,0}/t\right)^2$ with the parameters $l_{B_\perp} = 12$ nm and $a = 25$ nm. It is seen that the experimentally observed θ-dependence of the vertical conductance is reproduced by the theoretical curve with no adjustable parameters up to about $\theta = 30°$. Although the reduction of the interlayer transfer by the in-plane field is a physically sound model, the applicability of eq.(4.13) needs further assessment, because eq.(4.13) is derived for the bulk wave functions of Landau level, while the interlayer transfer in question is between the edge states.

To summarize the discussion in this section, we have observed a large positive transverse magnetoresistance of the chiral surface state. The transverse magnetoresistance of the chiral surface state is insensitive to the direction of the in-plane magnetic field. The semi-classical magnetoresistance as given by eq.(4.5) seems to be of minor importance. The major part of the observed magnetoresistance should be attributed to the suppression of interlayer transfer integral by the in-plane magnetic field.

Superlattice	Number of layers	Barrier width (nm)	Well width (nm)	Subband width $4t$ (meV)
A	100	15	10	0.12
B	50	12	10	0.42
C	50	10	10	0.95

Table 4.1: The important parameters of superlattice A, B and C

4.5 Comparison between superlattices

In this section, comparison between superlattices A, B and C is described. Because the values of interlayer transfer integral t differ for these superlattices, the comparison furnishes the information about the t-dependence of the chiral surface state.

In Fig.4.12, the magnetic field dependence of the out-of-plane resistance R_{zz} for three different superlattices with the same sample size (100×100 μm^2) are plotted. As the number of the 2D layers are different from superlattices, the vertical axis is normalized by the number of the 2D layers. The out-of-plane resistance R_{zz} increases rapidly at $\nu = 2$ and $\nu = 1$ in all samples. It was confirmed that the out-of-plane conductance G_{zz} at $\nu = 2$ is proportional to the mesa perimeter for all of them. Thus all the superlattices show qualitatively similar behavior.

The important parameters of these superlattices are listed in table 4.1. As the value of t increases from superlattice A to B and to C, one expects R_{zz} to decrease in this order. However the experimental result turned out otherwise, *i.e.* the superlattice B has the largest value of R_{zz}. This result indicates that the out-of-plane resistance R_{zz} at $\nu = 2$ is not scaled by single parameter t. As shown in eq.(4.1), R_{zz} depends on several unknown parameters of scattering time τ and edge velocity v. The unexpected result of the present experiments might be attributed to the substantial variance of these quantities from sample to sample. The considerable change of the MBE condition between superlattices may be also one of the reasons for the difference of quality of superlattices.

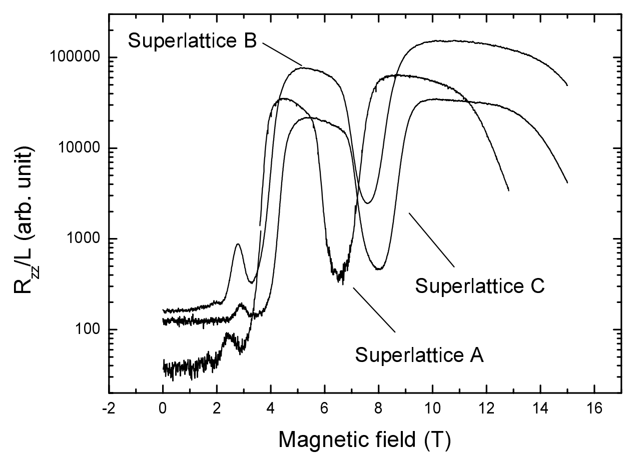

Figure 4.12: The magnetic field dependence of the out-of-plane resistance R_{zz} for three different superlattices with the same sample size (100×100 μm^2). As the number of the 2D layers are different from superlattices, the vertical axis is normalized by the number of the 2D layers.

Chapter 5

Conclusion

We have studied some aspects of the quantum Hall effect in semiconductor superlattices.

The quantum Hall state to Hall insulator transition in semiconductor superlattice is investigated. The magnetic field dependence and the temperature dependence of the longitudinal resistivity ρ_{xx} is analyzed in terms of the scaling theory. The critical exponent $\kappa = 0.30 \pm 0.05$ is obtained which is not significantly different from the purely two-dimensional case. The absence of metallic region near the critical region and the insensitivity to the in-plane magnetic field may suggest that each layer behave as individual 2DEG because of the small value of the interlayer transfer integral t.

In the quantum Hall state, the out-of-plane conductance G_{zz} and the in-plane diagonal resistance R_{xx} show similar temperature dependence above 200 mK, both decrease in Arrhenius-type temperature dependence with the activation energy $E_{\mathrm{a}} \sim 1$ K. This coincide may suggest that the relevant process for transport in both direction is the hopping conduction among the localized states in the tail of Landau subband.

The vertical conductance is proportional to the mesa perimeter at low temperatures in the quantum Hall regime. Distinct non-Ohmicity in the vertical transport is observed in this regime. The crossover from surface transport to bulk transport occurs as a function of the bias voltage. Non-Ohmic behavior in the high-voltage region can be interpreted in terms of the reduction of the effective activation energy. Smaller but substantial non-Ohmicity is also present in the low voltage (surface transport) regime, for which no simple explanation is given at the moment. The non-Ohmicity could be a clue to the elucidation of the marginally metallic character of the chiral surface state.

A large positive transverse magnetoresistance is observed in the vertical transport of the chiral surface state. It is insensitive to the direction of the in-plane magnetic field. The semi-classical magnetoresistance seems to be of minor importance. The major part of the observed magnetoresistance should be attributed to the suppression of interlayer transfer integral by the in-plane magnetic field.

References

[1] See, for example, "*The Quantum Hall Effect, Second Edition*", edited by R. E. Prange and S. M. Girvin (Springer-Verlag, 1990), "*Perspectives in Quantum Hall Effects*", edited by S. Das Sarma and A. Pinczuk (John Wiley & Sons, 1997).

[2] K. von Klitzing, G. Dorda, M. Pepper, Phys. Rev. Lett. **45** (1980), 494.

[3] B. I. Halperin, Phys. Rev. B **25** (1982), 2185.

[4] M. Büttiker, Phys. Rev. B **38** (1988), 9375.

[5] H. P. Wei, D. C. Tsui, M. A. Paalanen and A. M. M. Pruisken, Phys. Rev. Lett. **61** (1988), 1294.

[6] W. Pan, D. Shahar, D. C. Tsui, H. P. Wei and M. Razeghi, Phys. Rev. B **55** (1997), 15431.

[7] B. Huckenstein , B. Kramer and L. Schweitzer, Surf. Sci. **263** (1992), 125.

[8] M. Ya. Azbel, Phys. Rev. B **26**, 3430 (1982).

[9] B. I. Halperin, J. J. Appl. Phys. Suppl. **26** (1987) 1913.

[10] T. Ohtsuki B. Kramer and Y. Ono, J. Phys. Soc. Jpn. **62** (1993) 224.

[11] H. L. Störmer, J. P. Eisenstein, A. C. Gossard, W. Wiegmann and K. Baldwin, Phys. Rev. Lett. **56** (1985) 85.

[12] S. Hill, S. Uji, M. Takashita, C. Terakura, T. Terashima, H. Aoki, J. S. Brooks, Z. Fisk and J. Sarrao, Phys. Rev. B **58** (1998) 10778.

[13] J. R. Cooper, W. Kang, P. Auban, G. Montambaux, D. Jerome and K. Bechgaard, Phys. Rev. Lett. **63** (1989) 1984.

[14] S. T. Hannahs, J. S. Brooks, W. Kang, L. Y. Chiang and P. M. Chaikin, Phys. Rev. Lett. **63** (1989) 1988.

[15] J. T. Chalker and A. Dohmen, Phys Rev. Lett. **75** (1995) 4496.

[16] L. Balents and M. P. A. Fisher, Phys. Rev. Lett. **76** (1996) 2782.

[17] J. T. Chalker and S. L. Sondhi, Phys. Rev. B **59** (1999)4999.

[18] I. A. Grunzberg, N. Read and S. Sachdev, Phys. Rev. B **56** (1997) 13218.

[19] S. Cho, L. Balents and M. P. A. Fisher, Phys. Rev. B **56** (1997) 15814.

[20] V. Plerou and Z. Wang, Phys. Rev. B **58** (1998) 1967.

[21] J. J. Betouras and J. T. Chalker, Phys. Rev. B **62** (2000) 10931.

[22] D. P. Druist, P. J. Turley, K. D. Maranowski, E. G. Gwinn and A. C. Gossard, Phys. Rev. Lett. **80** (1998) 365.

[23] S. Uji, C. Terakura, M. Takashita, T. Terashima, H. Aoki, J. S. Brooks, S. Tanaka, S. Maki, J. Yamada and S. Nakatsuji, Phys. Rev. B **60** (1999) 1650.

[24] H. Yaguchi, N. Harrison, M. M. Honold, C. Mielke, J. Singleton, P. J. Gee, D. Rickel, I. Deckers, P. H. P. Reinders, F. Herlach, M. Kurmoo and P. Day, Physica B **251**(1998) 75

[25] L. L. Chang, H. Sakaki, C. A. Chang and L. Esaki Phys. Rev. Lett. **38** (1977) 1489.

[26] See, for example, "*The Technology and Physics of Molecular Beam Epitaxy*", edited by E. H. C. Parker (Plenum press, 1985).

[27] A 18 T superconducting magnet equipped with top-loading type dilution refrigerator at Tsukuba Magnet Laboratory, National Research Institute for Metals.

[28] D. Weiss, E. Stahl, G. Weimann, K. Ploog and K. von Klitzing, Surface Sci. **170** (1986) 285.

[29] A. Briggs, Y. Guldner, J. P. Vieren, M. Voos, J. P. Hirtz and M. Razeghi, Phys. Rev. B **27** (1983) 6549.

[30] Y. Ono, J. Phys. Soc. Jon. **51** (1982) 237.

[31] J. Hu and A. H. MacDonald, Phys. Rev. B **46** (1992) 12554.

[32] D. Yoshioka, J. Phys. Soc. Jpn. **64** (1995) 3168.

[33] D. B. Chklovskii, B. I. Shklovskii and L. I. Glazman, Phys. Rev. B **46** (1992) 4026.

[34] S. Takaoka, K. Otok H. Kurimoto, K. Murase, K. Gamo and S. Nishi, Phys. Rev. Lett **72** (1994) 3080.

[35] M. Kuraguchi and T. Osada, Physica E **6** (2000) 594-597.

[36] B. I. Shklovskii, Sov. Phys. Semicond. **6** (1973) 1964.

[37] D. P. Druist, E. G. Gwinn, K. D. Maranowski and A. C. Gossard, Physica E **6** (2000) 619.

Acknowledgement

I would like to express my best gratitude to the thesis supervisor, Prof. Y. Iye for the continual instruction and helpful suggestions and his critical reading of this manuscript. I am grateful to Prof. S. Katsumoto for valuable discussions. I would like to thank Dr. A. Endo for valuable discussions and kind help with semiconductor sample fabrication.

I would like to thank Prof. T. Ohtsuki for valuable discussions on the localization effect in the quantum Hall systems.

Some experiments were carried out in the 18 T superconducting magnet with a top-loading type dilution refrigerator at Tsukuba Magnet Laboratory, National Research Institute for Metals. I would like to thank Dr. S. Uji and Ms. C. Terakura for their experimental support at NRIM.

Finally, help and encouragement from every member of Iye-Katsumoto group are gratefully acknowledged.